

# Fluorescent Imaging Agents for Brain Diseases

Feida Che, Xiaoming Zhao, Xin Wang \*, Ping Li \* and Bo Tang

College of Chemistry, Chemical Engineering and Materials Science, Collaborative Innovation Center of Functionalized Probes for Chemical Imaging in Universities of Shandong, Key Laboratory of Molecular and Nano Probes, Ministry of Education, Institutes of Biomedical Sciences, Shandong Normal University, Jinan 250014, China; m15064108901\_1@163.com (F.C.); m19588902915@163.com (X.Z.); tangb@sdsu.edu.cn (B.T.)  
\* Correspondence: xinwang@sdsu.edu.cn (X.W.); lip@sdsu.edu.cn (P.L.)

**Abstract:** The onset of brain diseases has a terrible impact on people's lives, including brain tumors, Alzheimer's disease, Parkinson's disease, depression, and schizophrenia. Thus, the diagnosis and treatment of various brain disorders have been receiving specific attention. The fluorescence imaging technique is useful for examining brain diseases because it is intuitive, in situ, and real-time. Therefore, fluorescent imaging has so far been successfully employed to identify molecules associated with brain disease. In this review, the last five years of research advancements in fluorescent imaging agents for the above diseases are summarized, and the creation of pertinent fluorescence probes is described and prospected.

**Keywords:** brain tumors; Alzheimer's disease; Parkinson's disease; depression; schizophrenia; fluorescence imaging

## 1. Introduction

The brain is the physical center of the body, controlling not just speech, emotions, sensations, and so forth, but also the digestive, respiratory, circulatory, urinary, reproductive, and movement systems [1]. The brain is also the origin of all cognitive processes. The incidence of brain diseases, including brain tumors, Alzheimer's disease, Parkinson's disease, depression, and schizophrenia, might impact the brain's typical physiological function, which subsequently impacts how the human body functions on a daily basis [2]. Hence, the capacity to precisely identify or investigate the disease's mechanism is essential.

A variety of methods have been used to diagnose brain diseases or detect molecules associated with brain diseases, including proteomics [3,4], enzyme-linked immunosorbent assay (ELISA) [5,6], gel electrophoresis [7], immunohistochemistry (IHC) [8], immunofluorescence (IF) [9,10], and Western blotting [11,12]. These approaches, however, have some limitations, such as extended duration, invasive tissue injury, and difficulty achieving real-time detection and monitoring of biomarkers in situ.

Brain imaging technology may show the function and structure of the human brain in a non-invasive, indirect, or direct fashion, which is useful for diagnosing brain disorders and investigating the mechanisms of the occurrence and development of associated diseases [13–16]. Fluorescence imaging technology provides the benefits of high sensitivity, high selectivity, and real-time and in situ imaging of specific targets over other imaging techniques such as magnetic resonance imaging [17–19]. Especially exogenous fluorescence probes possessed selectivity, specificity, and high sensitivity for bioactive molecules that are abnormal during the occurrence and development of brain diseases. By unitizing those high-selectivity fluorescence probes, the researchers could investigate the molecular mechanisms of diseases in living cells and in vivo. Therefore, researchers have created a variety of fluorescence imaging tools to investigate the chemicals implicated in brain disorders [20,21]. Small molecule fluorescence probes and nanofluorescence probes offer great photostability, high resolution, and a large fluorescence quantum yield, and they may use different dye



**Citation:** Che, F.; Zhao, X.; Wang, X.; Li, P.; Tang, B. Fluorescent Imaging Agents for Brain Diseases. *Targets* **2023**, *1*, 5–33. <https://doi.org/10.3390/targets1010003>

Received: 29 April 2023

Revised: 27 May 2023

Accepted: 30 May 2023

Published: 1 June 2023



**Copyright:** © 2023 by the authors. Licensee MDPI, Basel, Switzerland. This article is an open access article distributed under the terms and conditions of the Creative Commons Attribution (CC BY) license (<https://creativecommons.org/licenses/by/4.0/>).

molecules to satisfy the demands of diverse conditions [22,23]. These fluorescent probes have greatly aided researchers looking into the causes of neurological disorders.

This paper primarily reviews the last five years of published fluorescence imaging work related to brain tumors, Alzheimer's disease, depression, Parkinson's disease, and schizophrenia, and discusses and forecasts the development of new fluorescence probes and the establishment of fluorescence imaging methods, which are expected to provide technical support for a comprehensive understanding of the occurrence and progression of related brain diseases.

## 2. Brain Tumors

There are numerous varieties of brain tumors, such as gliomas, meningiomas, acoustic neuromas, etc. Gliomas predominate among brain tumors, with glioblastoma being the most prevalent malignant histological subtype [24]. Early symptoms of brain tumors may not be evident, resulting in a late diagnosis, difficult treatment, and significant patient suffering. Therefore, early detection of gliomas and other brain tumors can increase the rate of healing. The advantages of fluorescence imaging include noninvasiveness, in situ diagnosis, real-time diagnosis, etc. Researchers have, therefore, devised a variety of fluorescent dyes for the early diagnosis and effective treatment of brain tumors.

Second near-infrared region (NIR-II) imaging has the advantages of high spatial and temporal resolution, high sensitivity, less background interference, and so on [25,26]. It also has great advantages in the imaging diagnosis of brain tumors. Therefore, there is a lot of excellent work in NIR-II. Wu and co-workers developed a fluorination strategy for the development of highly fluorescent polymers (Figure 1, 1) in NIR-II [27]. By using benzodithiophene (BDT) and triazole[4,5g]-quinoxaline (TQ) derivatives as donors and acceptors, they created two sets of fluorine-substituted semiconductor polymers. **1** exhibited bright fluorescence. Through skull and scalp imaging of the cerebrovascular system of live mice, they quantitatively analyzed the vascular morphology of the transgenic brain tumors, such as vascular length, vascular branching, and vascular symmetry. This strategy is critical for designing NIR-II fluorophores with greater fluorescence and provides an important tool for reliable brain tumor diagnosis.

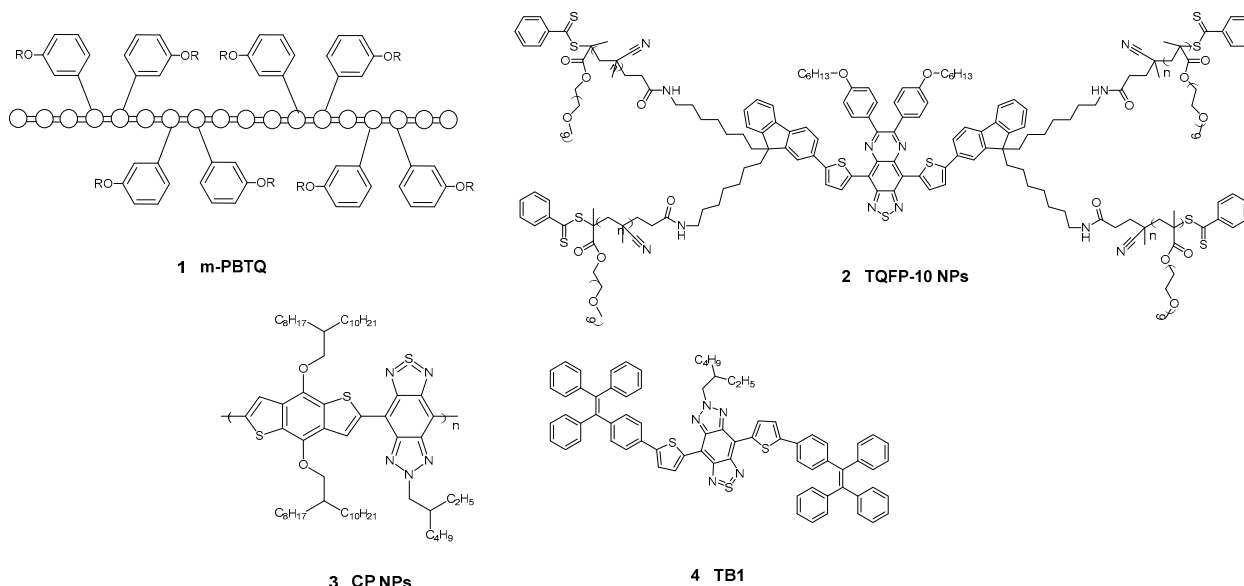


**Figure 1.** Chemical structure of brain tumor imaging materials.

Fan and co-workers developed small-size nanoparticles, TQFP-10 NPs (Figure 1, 2) (~8 nm), with NIR-II fluorescence emission for orthotopic glioblastoma imaging [28]. Precise synthesis of the POEGMA brush arms of TQFP-10 via RAFT polymerization ensures high water solubility and a controlled ultrasmall particle size. **2** possessed bright NIR-II fluorescence and an excellent blood circulation half-life. Therefore, this work provides

a new method for constructing the ideal nanoparticle of NIR-II fluorescence to achieve effective imaging of orthotopic glioblastoma.

Li et al. created  $\text{NaNdF}_4$ -based nanoparticles with robust NIR-II fluorescence for imaging orthotopic glioblastomas [29]. The  $\text{NaNdF}_4$  nanoparticles were coated with an inert layer of  $\text{NaLuF}_4$  and then sensitized with a near-infrared dye (IR-808), which resulted in a 10-fold increase in their conventional emission (Figure 2). Using focused ultrasound, these nanoparticles can be efficiently delivered to tumor tissue, thereby temporarily opening the blood–brain barrier (BBB) in mice. Compared to 1060 nm fluorescence, in vivo imaging emitted at 1340 nm possesses a higher signal-to-noise ratio and deeper penetration. Both fluorescence imaging and sparse soil staining of brain tissue further confirmed the accumulation of nanoparticles within the tumor. The work demonstrates the potential of dazzling dye-sensitized rare earth nanoparticles in the diagnosis of glioblastoma and provides guidance for enhancing neglected NIR-II imaging with feeble long-wavelength fluorescence.

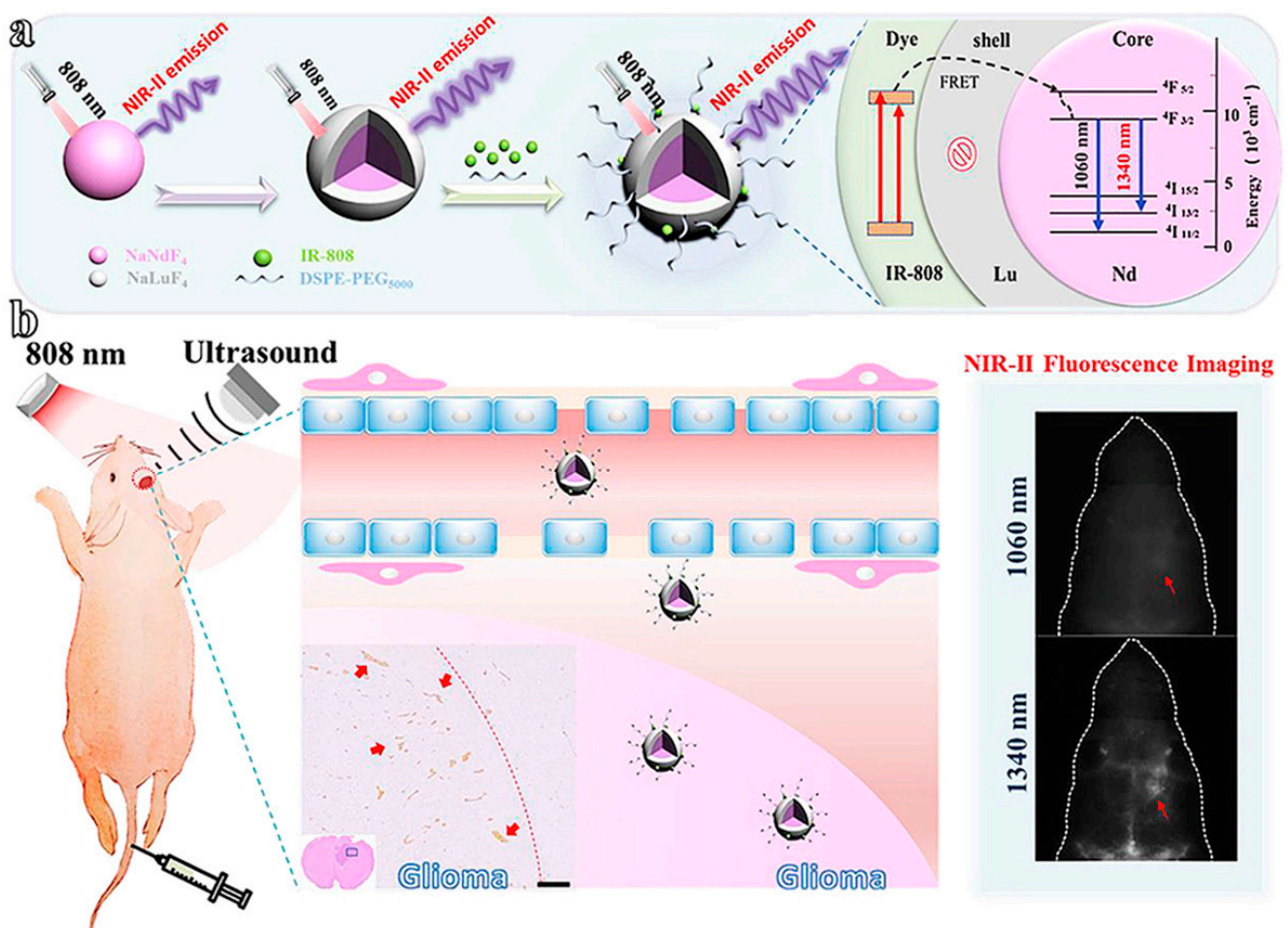


**Figure 2.** (a) Schematic illustration of the synthesis of water-soluble dye-sensitized core-shell  $\text{NaNdF}_4@NaLuF_4/IR-808@DSPE-PEG5000$  NPs and their energy transfer mechanism. (b) Application of the core-shell  $\text{NaNdF}_4@NaLuF_4/IR-808@DSPE-PEG5000$  NPs in NIR-II fluorescence imaging of orthotopic glioblastoma under ultrasound-mediated opening of the BBB, and rare-earth staining of brain tissue after delivery into the brain [29].

Li et al. reported an energy-cascaded strategy for enhancing the NIR II emission of Er-based core-shell-shell down-conversion nanoparticles (DCNPs), which are used for targeted imaging and image-guided surgery for orthotopic gliomas [30]. They modified the optimal DCNPs with dye-brush polymer (Dye-BP) to facilitate  $^4I_{13/2} \rightarrow ^4I_{15/2}$  transition. Then, they modified nanoparticles with tumor-targeting angiopep-2 peptide (ANG), which can specifically bind to overexpressed low-density lipoprotein receptor-related protein

(LRP) on glioma cells (Figure 3). Fluorescence emission of DCNPs in aqueous solution at 1525 nm was increased 675-fold. Moreover, DCNPs exhibit potent fluorescence emission and profound tissue penetration. Altogether, DCNPs exert tremendous potential for imaging deep tumors and image-guided surgery.

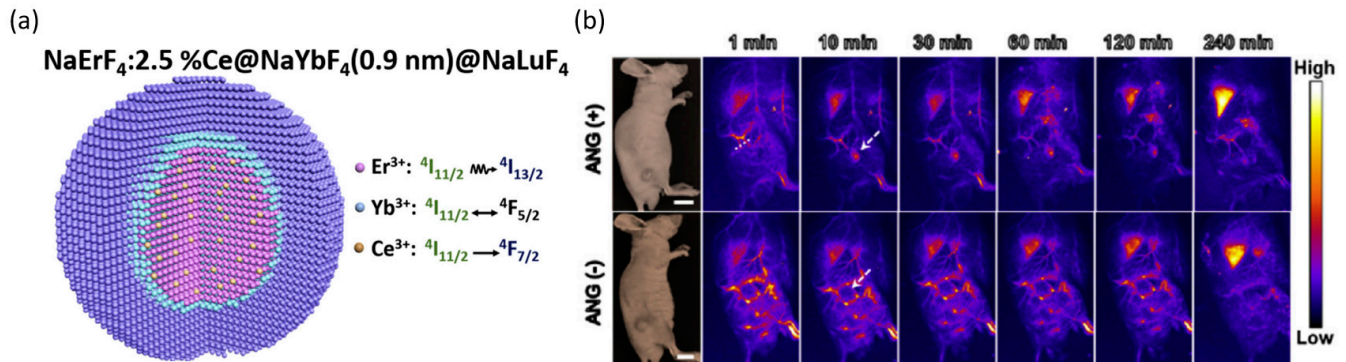


**Figure 3.** (a) Composition of DCNPs. (b) Bright-field and NIR IIb fluorescence images of subcutaneous gliomas from mice intravenously injected with Er-DCNPs-Dye-BP and Er-DCNPs-Dye-BP-ANG [30].

Multifunctional materials have the advantages of performing multiple functions and being more comprehensive. Therefore, numerous efforts were devoted to the development of multifunctional imaging materials. Li and co-workers created a macrophage loaded with a photothermal nano-probe (MFe<sub>3</sub>O<sub>4</sub>-Cy5.5) that can conduct magnetic resonance imaging (MRI), fluorescence imaging (FLI), and photoacoustic imaging (PAI) on primary macrophages and target gliomas in mice after injection into the tail vein [31]. Cy5.5 was conjugated onto the surface of the nanoparticles, which was then taken up by primary macrophages (Figure 4). After injection into the tail vein, MFe<sub>3</sub>O<sub>4</sub>-Cy5.5 could cross the blood–brain barrier and reach glioma cells. Multimodal imaging of glioma cells could be used to guide surgical excision, while postoperative tumors could be treated with photothermal therapy. Satisfyingly, MFe<sub>3</sub>O<sub>4</sub>-Cy5.5 exhibits distinguished imaging depth, a high signal-to-noise ratio, and an excellent photothermal treatment effect. Altogether, utilizing macrophages containing safe and effective porous magnetic nanoparticles of iron oxide to diagnose and treat gliomas has significant potential applications.

Liu and co-workers reported the use of organic contrast agents (Figure 1, 3) for brain tumor diagnostics with dual NIR-II fluorescence and photoacoustic (PA) imaging capabilities [32]. 3 exhibits superior biocompatibility and photostability, and can display high-resolution images of deep cerebral blood vessels and blood flow in real time. 3 images advanced brain tumors by the enhanced permeability and retention (EPR) effect. Altogether, 3 has a promising application for dual NIR-II fluorescence and photoacoustic imaging, as well as the potential for future image-guided real-time neurosurgery and photothermal therapy.

To create stable nanoagents for extremely sensitive multimodal imaging and photothermal therapy of brain malignancies, Liu's group encapsulated near-infrared compounds (TC1) in nanocomposites with ultrasmall iron oxide nanoparticles (UIONPs) [33]. To mitigate the fluorescence suppression caused by the adjacent region between UIONPs and TC1, they effectively prepared HALF, which created a spatial separation between the two components (Figure 5). In addition, survival rates of brain tumor-bearing mice treated with photothermal therapy-assisted HALF-cRGD (cRGD: Arg-Gly-Asp-Phe-Lys) were significantly higher than those of other groups. This work demonstrates the benefits of carefully designed multimodal imaging contrast agents, thereby shedding light on the overall performance design considerations for multifunctional therapeutic nanoagents.

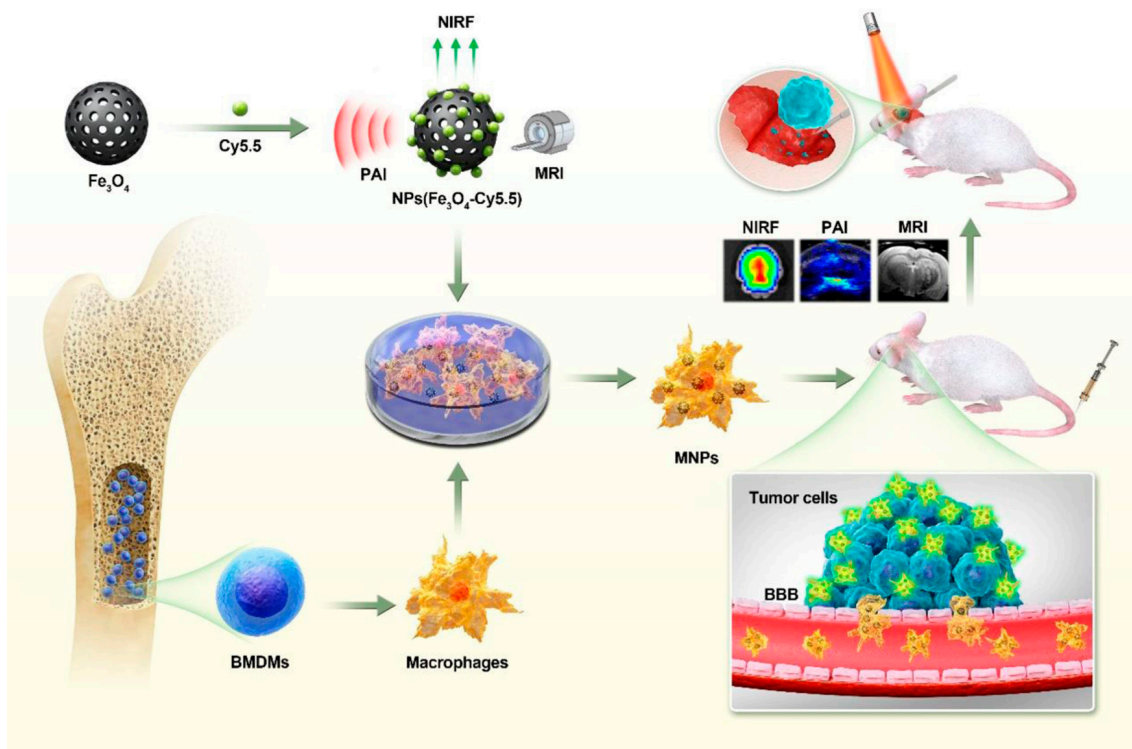


**Figure 4.** Synthesis process and application of  $MFe_3O_4-Cy5.5$ . Macrophages loaded with  $Fe_3O_4-Cy5.5$  were used for multimodal imaging to help in the accurate diagnosis of gliomas, guide surgical resection, and perform postoperative photothermal therapy [31].

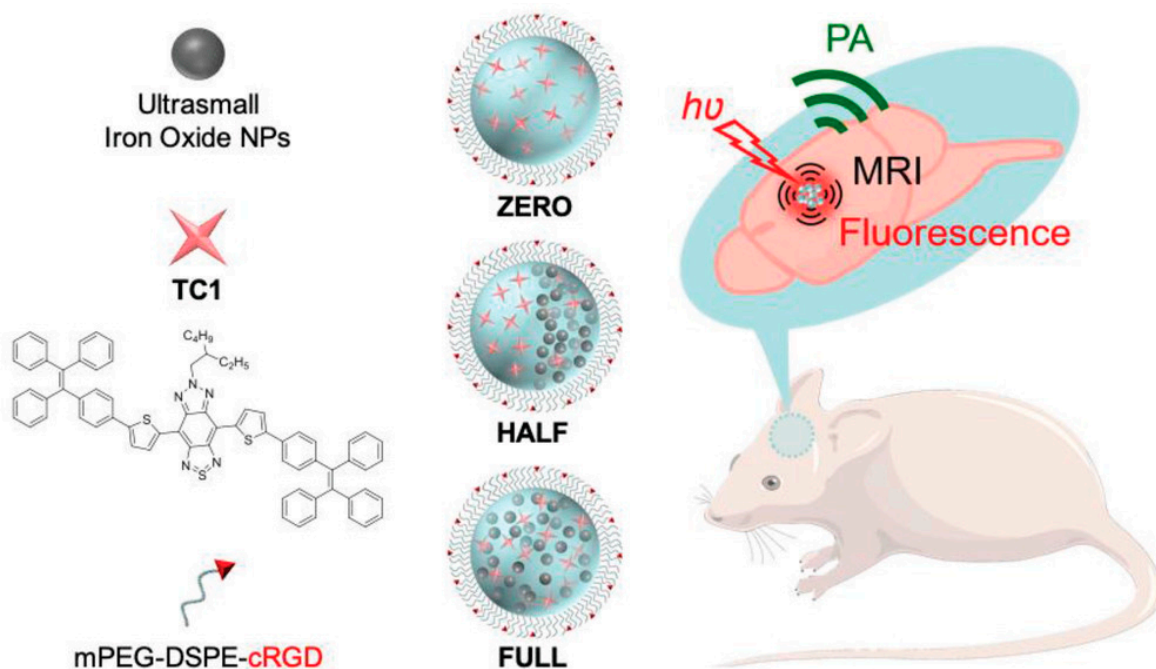


**Figure 5.** Schematic illustration of the nanostructures of ZERO, HALF, and FULL nanocomposites and multimodal brain tumor imaging applications [33].

Yang et al. report a protein-based molecular imaging probe (RGD-RFP-LBT-Gd) for tumor-targeted FL/MR imaging [34]. The RGD-RFP-LBT was obtained by integrating the tumor-targeted Arg-Gly-Asp (RGD) peptide, red fluorescence protein (RFP), and

lanthanide-binding tag (LBT) (Figure 6). The probe possessed superior imaging capabilities in physiological environments, including sustained fluorescence emission, a broad pH range, and superior T1-weighted magnetic resonance imaging capabilities compared to commercially available GdDTPA. The probe showed excellent biocompatibility and fluorescence/magnetic resonance imaging performance in tumor-bearing mice. Therefore, this work provides a general strategy for the design of multimodal protein molecular imaging probes and encourages the development of molecular imaging probes for disease diagnosis.

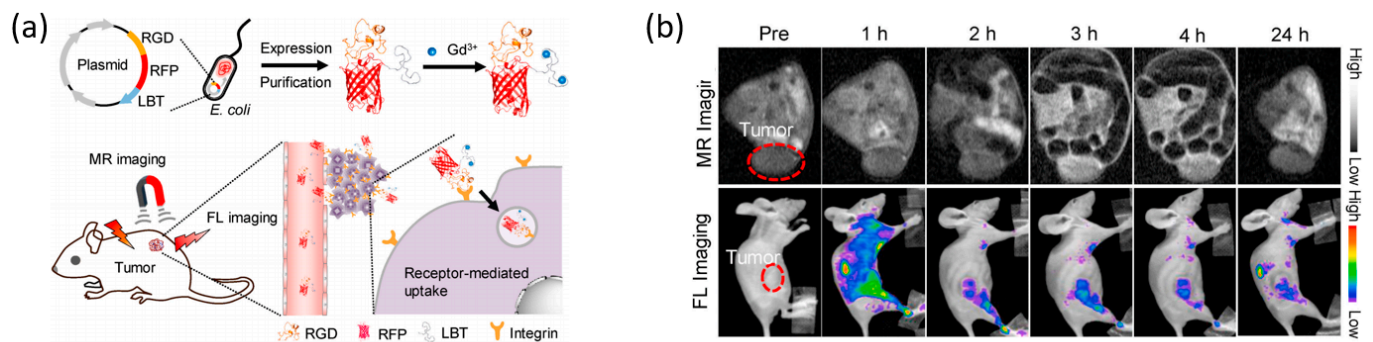


**Figure 6.** (a) Schematic overview of the biosynthesis of a protein-based molecular imaging probe (RGD-RFP-LBT-Gd) for tumor-targeted FL/MR imaging. (b) MR and FL imaging photos of representative tumor-bearing mice intravenously injected with RGD-RFP-LBT-Gd at different times (0, 1, 2, 3, 4, and 24 h) [34].

Due to their unique properties, aggregation-induced emission (AIE) materials have numerous applications and also play a crucial role in imaging brain tumors. Liu and co-workers designed a new donor–acceptor (D–A)-tailored NIR-II emissive AIE molecule TB1 (Figure 1, 4) for brain tumor diagnosis [35]. Encapsulating the molecule in a polymer matrix produces AIE dots with an extremely high fluorescence quantum yield (QY) of 6.2%. 4 could target tumors by introducing c-RGD. The higher NIR absorption of 4 facilitates NIR-I photoacoustic imaging, which essentially has deeper penetration than NIR-II fluorescence imaging, enabling accurate tumor depth detection through the intact skull. The bright 4 holds tremendous potential for monitoring and visualizing cerebrovascular and brain tissue abnormalities, as well as for accurate diagnosis of brain tumors.

Sheng and co-workers employed endogenous albumin as an efficient matrix for encapsulating AIEgens to enhance fluorescence QY and active targeting ability [36]. The hydrophobic domain of albumin interacts strongly with AIEgens and immobilizes proteins via hydrogen bonding, inhibiting the intramolecular vibration of AIEgens and enhancing QYs (Figure 7). The albumin-based AIE nanoprobes exhibited higher QYs and cell uptake efficacy than traditional DSPE-PEG2000-based AIE nanoprobes. In vivo, using albumin-based AIE nanoprobes, the authors can obtain high signal-to-background ratio (SBR) (~90) and high resolution (~70  $\mu\text{m}$ ) for brain tumors and cerebral ischemia by NIR-II fluorescence imaging. Altogether, this work provides a new method for designing high-quality AIEgens for application in brain imaging.

Jiang and colleagues created a two-photon fluorescent probe that can detect and image hyaluronidase (HAase) in cancer cells using a combination of graphitic carbon nitride (g-CN) nanosheets and a nano-assembly of hyaluronic acid (HA)-coated gold nanoparticles (HA–AuNPs) [37]. The nanoplatform involves the assembly of positively charged g-CN nanosheets with negatively charged HA–AuNPs, which results in the quenching of g-CN nanosheet fluorescence through electrostatic and hydrophobic interactions. HAase degraded HA into low molecular weight fragments and separated g-CN nanosheets from HA–AuNPs, thereby restoring the fluorescence of g-CN nanosheets (Figure 8). This probe enables high-sensitivity, specific detection, and two-photon imaging of HAase in cancer cells and deep tissues. This work could provide a promising platform for high-specificity and high-sensitivity imaging of HAase and associated cancer diagnosis.

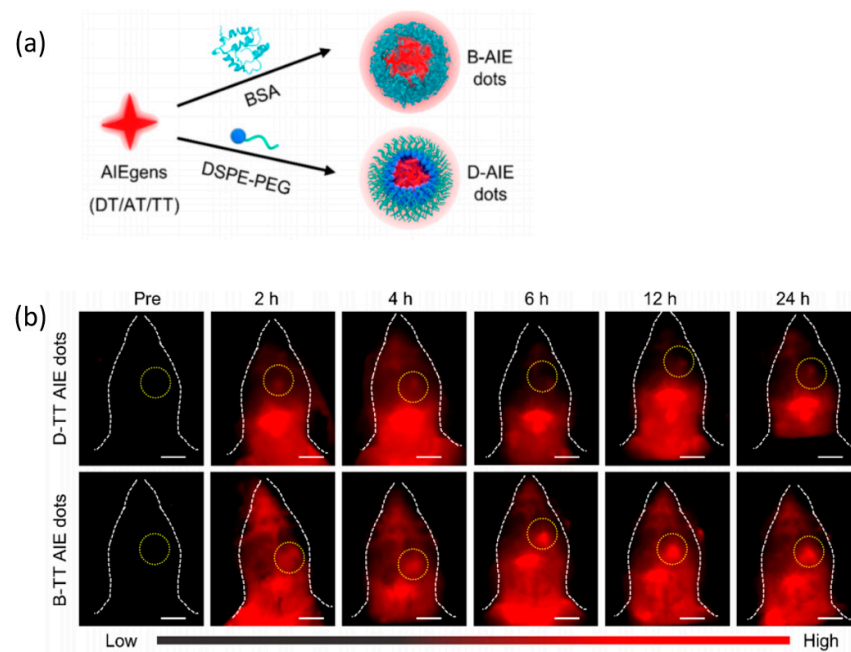


**Figure 7.** (a) Composition of AIEgens. (b) NIR-II FL imaging of C6 tumor-bearing mice after administration of B-TT AIE dots and D-TT AIE dots at different time points [36].

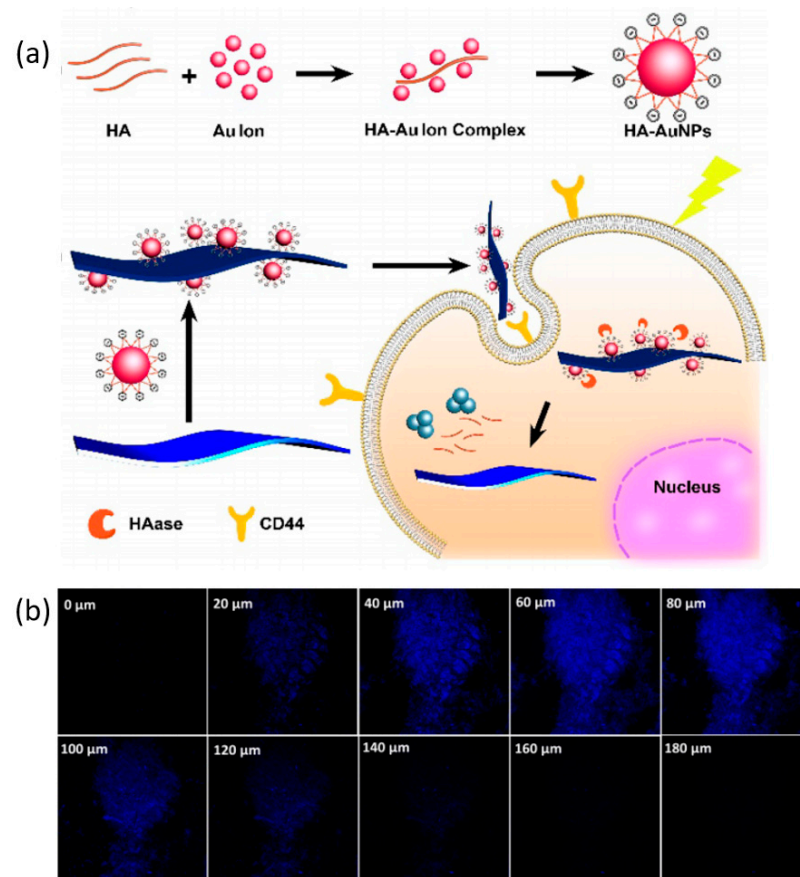


**Figure 8.** (a) Schematic illustration of the synthetic process of HA–AuNPs and application of the prepared HA–AuNPs/g-CN nanoassembly as an efficient platform for activatable two-photon fluorescence imaging. (b) Depth fluorescence images of the nanoassembly in MDA-MB-231 cancer tissue slices. The change of fluorescence intensity with scan depth was determined by spectral confocal multiphoton microscopy in the z-scan mode [37].

### 3. Alzheimer's Disease

Alzheimer's disease is a neurodegenerative disease commonly characterized by memory deficits and cognitive decline. The main biomarkers currently used to diagnose the disease are beta-amyloid plaques, phosphorylated tau, and the presence of neurofibrillary tangles [38]. With the exception of a few familial diseases driven by genetic mutations, the mechanisms of Alzheimer's disease are not completely understood. Therefore, it is essential to develop effective diagnostic tools and disease-modifying therapies for Alzheimer's disease. For the diagnosis of Alzheimer's disease, researchers have conducted extensive work on imaging biomarkers such as amyloid protein (A) and peroxynitrite over the past five years.

A $\beta$  is a polypeptide containing 39~43 amino acids produced by the hydrolysis of amyloid precursor protein (APP) by  $\beta$ - and  $\gamma$ -secretase [39,40]. A $\beta$  deposition is associated with the development and progression of Alzheimer's disease. A $\beta$  comes in a variety of forms, such as monomers (single peptide units), oligomers, aggregates, plaques, hexamers, ninomers, fibrils, and amyloid plaques [41]. For multispectral photoacoustic and fluorescence imaging of A $\beta$  in the AD brain, Klohs et al. employed CRANAD-2 (Figure 9, 5), a derivative of curcumin [42]. 5 exhibited specific and quantitative detection of A $\beta$  fibrils in vitro, and it can distinguish between monomeric and fibrillar forms of A $\beta$ . Immunohistochemistry revealed that 5 and A $\beta$  fibrils were co-localized in arcA $\beta$  mouse brains, validating the probe's specificity. This work demonstrates the applicability of 5 for optical detection of A $\beta$  deposits in mouse models of AD pathology, which might be helpful in mechanism investigations and monitoring of potential therapies against A $\beta$  deposits. This method will facilitate the identification of disease pathways in mice and the longitudinal monitoring of A $\beta$ 's therapeutic effects.

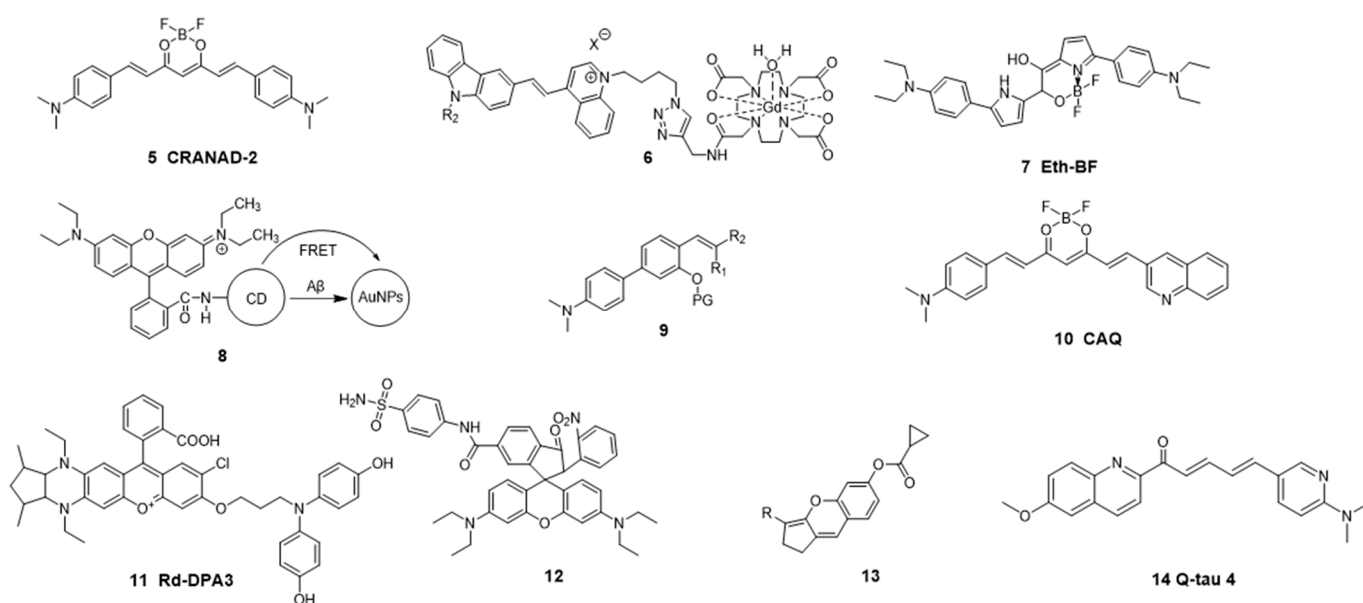


**Figure 9.** Chemical structure of the imaging materials for Alzheimer's disease.

Wong and co-workers developed a multimodal contrast agent (Figure 9, 6) for in vivo and in vitro imaging of A $\beta$  in the brains of mice with AD [43]. 6 could cross the blood-brain barrier (BBB) and specifically target A $\beta$ . 6 realized NIR-II fluorescence, two-photon fluorescence, and MR imaging of A $\beta$  in AD mouse models. In addition, 6 was also able to effectively inhibit self-aggregation of A $\beta$ , thereby preventing A $\beta$ -induced toxicity, as well as inhibit reactive oxygen production, indicating its potential as an A $\beta$ -tagged therapeutic agent for diagnosis and treatment. This work also highlights the extraordinary potential of the effective and sensitive contrast agent for multimodal imaging of human A $\beta$ .

Based on a rhodamine–copper complex, Gong and co-workers developed a fluorescent probe for the detection of A $\beta$ 42 to distinguish AD mice from normal mice [44]. They selected rhodamine as the fluorophore and used four different Cu<sup>2+</sup> chelate parts as the recognition unit of A $\beta$ 42. The fluorescence of rhodamine was quenched due to the photoinduced electron transfer (PET) effect (Figure 10). When Cu<sup>2+</sup> chelates with A $\beta$ 42, the PeT effect is interrupted and the fluorescence is restored. The probe showed high sensitivity (detection limit = 24 nM), high affinity (K<sub>d</sub> = 23.4 nM), high selectivity, and a fast response speed (within 1 min). Furthermore, utilizing two-photon fluorescence imaging, Rho4-Cu could image A $\beta$ 42 in APP/PS1 transgenic mice. These promising results indicated that the probe possesses great potential for the future diagnosis of AD.

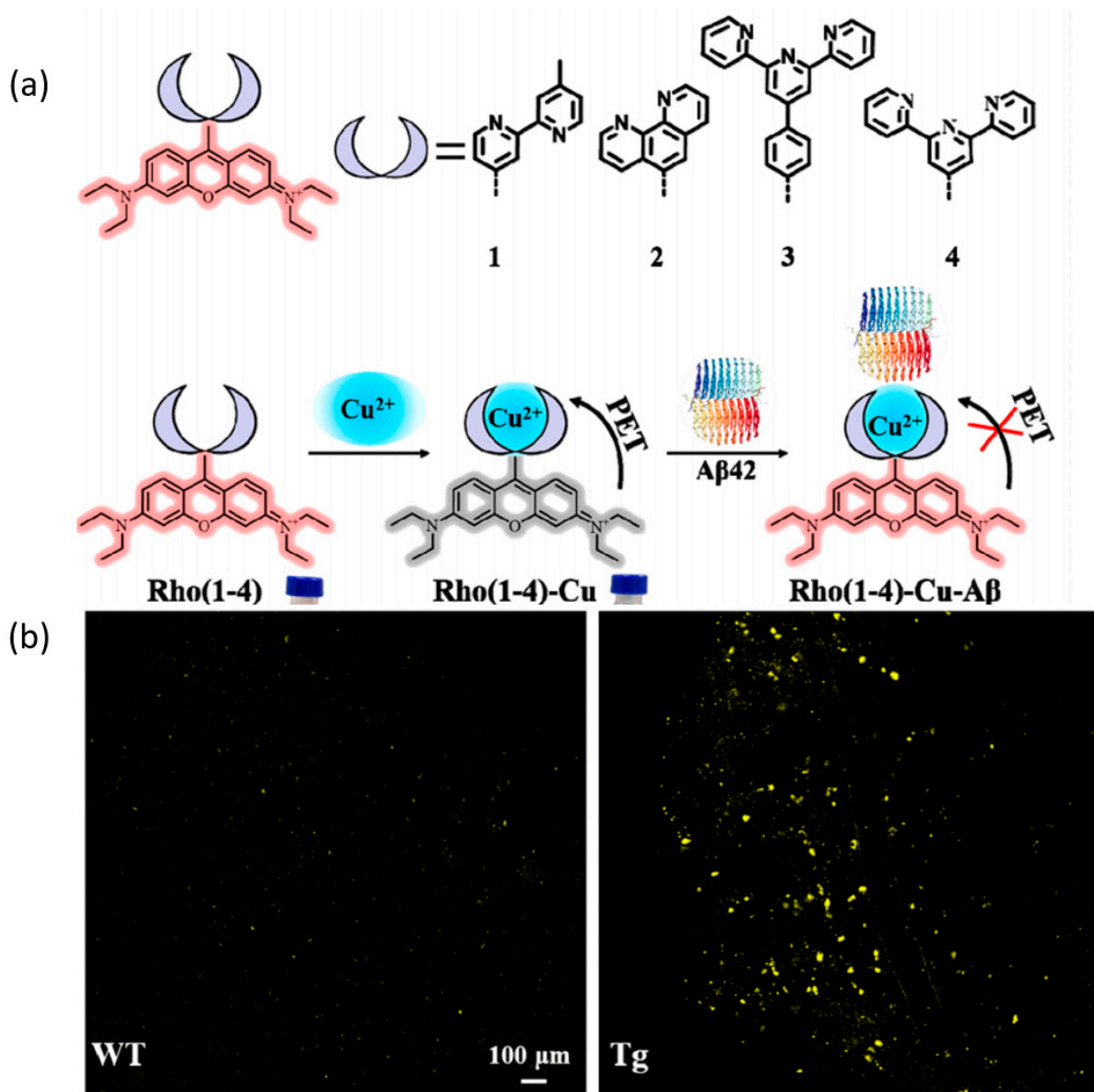


**Figure 10.** (a) Design strategy and structure of the compounds with a Cu<sup>2+</sup> chelating moiety for A $\beta$ 42 (b) Two-photon fluorescence imaging of the brain in wild-type mice (WT) and APP/PS1 mice (Tg) by Rho4 [42].

Pan and co-workers designed and synthesized a NIR-II fluorescence probe, Eth-BF (Figure 9, 7), for A $\beta$  oligomers imaging [45]. 7 consists of N, N-diethylaniline as the recognition group and boron difluoride-bridged azafluorene as the electron-absorbing group. Due to the intramolecular charge transfer (ICT) effect, the fluorescence emission of 7

redshifts to the NIR-II region. Moreover, **7** is sensitive to ambient viscosity, achieving high sensitivity and accuracy of fluorescence switch emission via the AIE process. **7** showed high sensitivity ( $K_d = 6.16$  nM) for the detection of A $\beta$  oligomers. The low molecular weight of **7** facilitates rapid penetration of the blood–brain barrier and imaging of A $\beta$  oligomers in 3-month transgenic AD mouse models. Altogether, **7** is a promising tool for the early diagnosis of AD.

Salimi and co-authors synthesized a probe (Figure 9, **8**) to measure the levels of A $\beta$  peptide in SH-SY5 neuroblastoma cells [46]. **8** is a hybrid conjugate comprising rhodamine B (RB), carbon dots (CDs), and an A $\beta$ -specific probe entrapped in polyvinyl alcohol (PVA). Hybridization leads to the occurrence of fluorescence resonance energy transfer (FRET) when AuNP/target-A $\beta$  is present. A $\beta$ -antibody modification of **8** allowed for selective interaction with A $\beta$ . Upon excitation at 430 nm, **8** produced fluorescence at both 582 nm and 675 nm. The strong coordination between RB-CDs and A $\beta$  antibody resulted in a decrease in the red emission (675 nm) and an increase in the green emission (582 nm) after the addition of A $\beta$  peptide. Consequently, the  $I_{582}/I_{675}$  ratio changed with variations in A $\beta$  concentration. Compared with other interferors, this method is more selective for A $\beta$  and is applicable to human serum samples. In addition, **8** was able to accurately image A $\beta$  in both stationary and living neuroblastoma SH-SY5 cells. With the benefits of simplicity, low cost, and absence of interference, the biosensor could be used at the point of care to diagnose AD biomarkers.

Wang and co-workers developed a photo-triggered fluorescent probe, PTAD-3 (Figure 9, **9**), for A $\beta$  aggregates [47]. The 6-nitroveratry group was selected as the photoremoval protective group. Under light irradiation, the probe PTAD could be transformed into the faint fluorescent compound PTAD-C by releasing the photoremovable protecting group and conducting a cyclization reaction. PTAD-C could bind with A $\beta$  aggregates to generate strong fluorescence, thus realizing the light-controlled detection of A $\beta$ . PTAD-3 could be used to detect A $\beta$  aggregates in AD model (APP/PS1 transgenic) mice with blood–brain barrier permeability (Figure 11). This strategy could be applied to design various photo-trigger probes for detecting specific proteins with a high signal-to-noise ratio.

Qian and co-workers report a NIR fluorescent probe CAQ (Figure 9, **10**) for selective imaging of A $\beta$  aggregates in vivo [48]. CAQ was synthesized by modifying curcumin with 4-(dimethylamino)-benzaldehyde and 3-quinolinecarboxaldehyde, followed by boron di-fluoride treatment. The probe's weak emission intensity at low viscosities can be attributed to the intramolecular rotation effect, but its fluorescence is significantly enhanced in high-viscosity environments. CAQ can be used for NIR imaging in brain tissues, *Caenorhabditis elegans*, and  $5 \times$  FAD mouse models with early A $\beta$  deposition. Therefore, the probe has the potential to be utilized in future clinical diagnosis with further modification.

Peroxynitrite (ONOO $^-$ ) is a typical species of oxidative stress response and plays an important role in the pathogenesis of AD through neurotoxicity and neuroinflammation [49]. Our group has developed a two-photon fluorescence probe, BTNPO, that can be used for two-channel detection of A $\beta$  plaques and ONOO $^-$  [50]. BTNPO consists of a typical donor-recipient dipole structure with a highly rotating single bond in the middle (Figure 12). We simultaneously observed the distribution and change of A $\beta$  plaques and ONOO $^-$  by BTNPO. In the mouse model of AD, we found that brain ONOO $^-$  can be used as a potential biomarker to determine the progression of AD. BTNPO has the potential to explore the mechanisms of disease signaling associated with ONOO $^-$  and A $\beta$  plaques.

To study the complex relationship between peroxynitrite and AD, Kim and co-workers designed an ONOO $^-$ -activated NIR fluorescent probe, Rd-DPA3 (**11**) [51]. **11** is composed of the diamino-substituted Rhodol dye NIR-Rd-3 as the fluorophores, with the 4-aminophenol group serving as the ONOO $^-$  distinguishing group. **11** realized in situ imaging of ONOO $^-$  in AD mice for the first time. This work further supports ONOO $^-$  as a biomarker for AD, providing a new direction for the design of ONOO $^-$  probes and the diagnosis of AD.

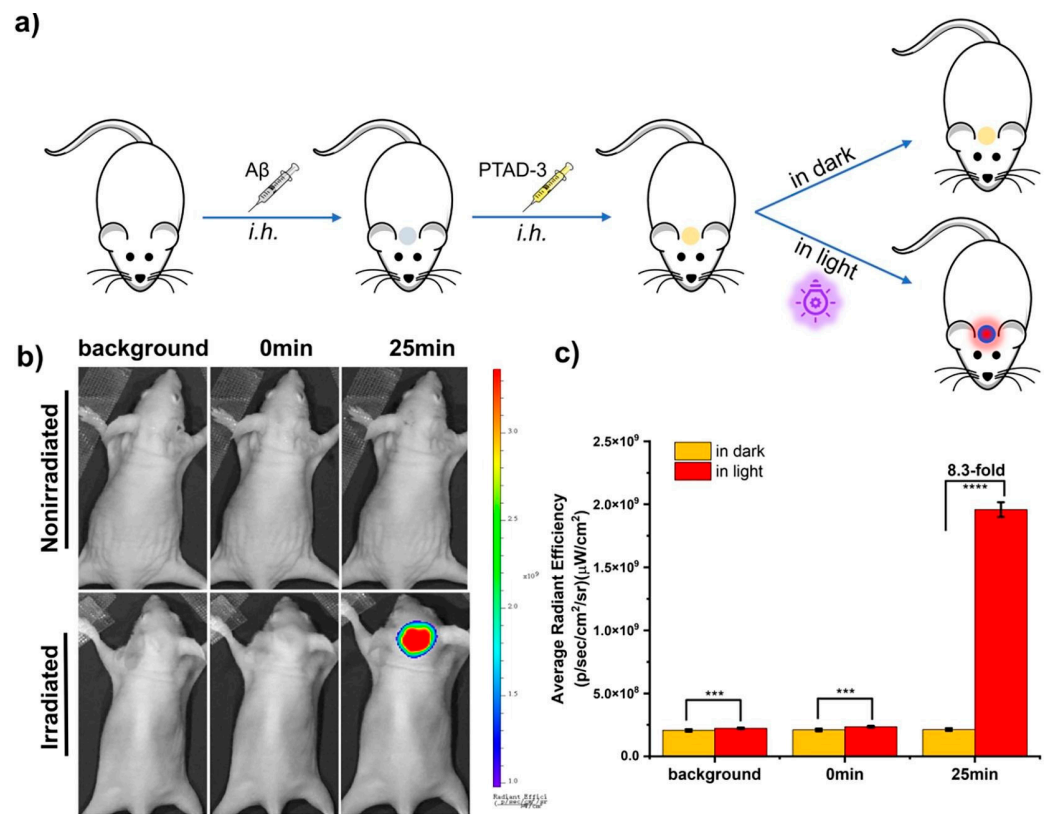


**Figure 11.** (a) Schematic diagram of  $A\beta$  imaging with PTAD-3 in vivo in the simulation model (i.h. means hypodermic injection); (b) In vivo images of nude mice at 25 min after the hypodermic injection of PTAD-3 ( $2.0 \text{ mg/kg}^{-1}$ ), which were with or without irradiation under 365 nm UV,  $n = 3$ ; (c) Quantification of the mean ratio of fluorescence intensity in b. \*\*\*  $p < 0.001$ , \*\*\*\*  $p < 0.0001$  [47].

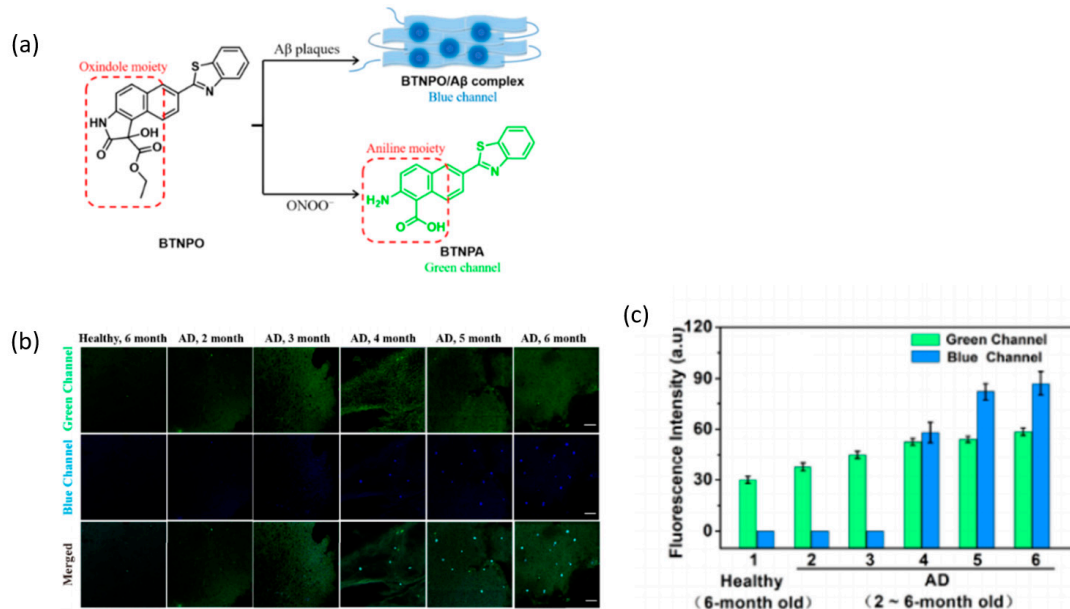


**Figure 12.** BTNPO was injected into healthy and APP/PS1 transgenic AD mice, and the hippocampus region was isolated and sectioned into slices for two-photon fluorescence imaging. (a) Dual-color fluorescence responses of BTNPO to  $A\beta$  plaques and  $ONOO^-$  (b) Coimaging of  $ONOO^-$  (green channel) and  $A\beta$  plaques (blue channel) in the brain hippocampus of healthy and AD mice. (c) The average fluorescence intensities of the blue and green channels in (a) were quantified [50].

Ma and co-workers designed and synthesized Golgi-NO (**12**) as a Golgi-targeted fluorescent probe to detect NO in AD mice [52]. **12** consists of 6-carboxyrhodamine B as the fluorophore, 4-sulfamoylphenylamide as the group targeting the Golgi apparatus, and *o*-diaminobenzene as the 2-carboxyl of Golgi-RhB for sensing NO. **12** has excellent Golgi targeting ability and can specifically detect NO. Using Golgi-NO, they found a significant increase in NO in the Golgi apparatus during A $\beta$ -induced AD. This study provides a valuable tool for in situ imaging of NO in the Golgi apparatus and for exploring the role of NO in disease-related signaling pathways.

Xu and co-workers reported a biocompatible Fe<sub>3</sub>O<sub>4</sub> nanoparticle (IONP)-conjugated methylglyoxal(MGO)-activatable NIR-II fluorescent probe (MAM) modified with the peptide T7 (HAIYPRH) (TM-IONP) for in situ detection of MGO in transgenic AD mice [53]. They developed an organic NIR-II fluorescent probe with an MGO-activated response and then attached it to the surface of a biocompatible Fe<sub>3</sub>O<sub>4</sub> nanoparticle to create water-dispersible nanoparticles (IONP). The T7 peptide was utilized to enhance BBB crossing and brain accumulation (Figure 13). TM-IONP has high sensitivity (detection limit = 72 nM) and can detect subtle abnormalities in the level of MGO in the AD brain, allowing it to distinguish AD mice from normal mice. This nanoprobe activated by MGO represents a potential application in the early clinical diagnosis of AD.

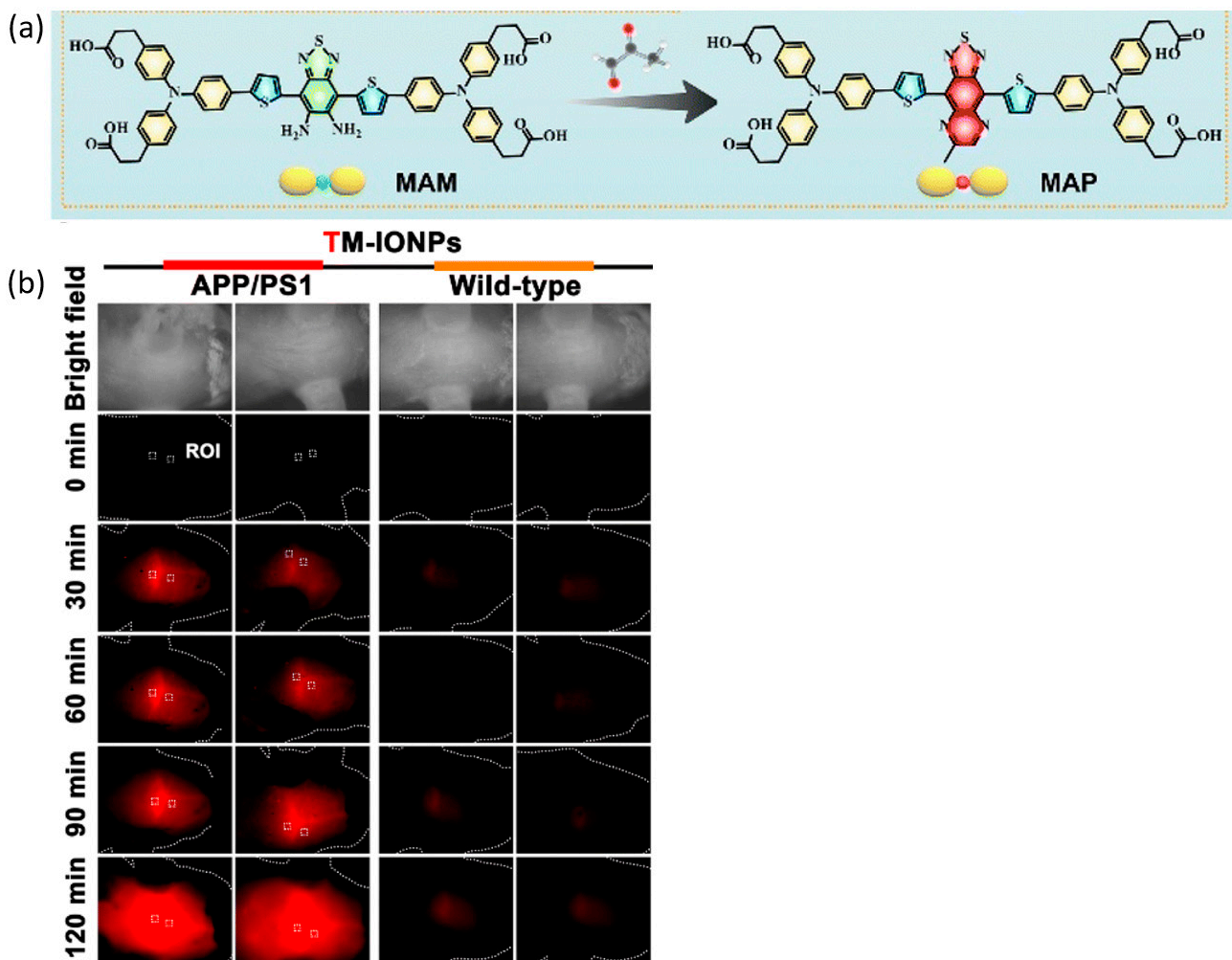


**Figure 13.** (a) Amplification of the response mechanism of MAM towards MGO in living cells. (b) Representative in vivo/ex vivo NIR-II fluorescence imaging of the brains of TM-IONP-treated APP/PS1 mice and TM-IONP-treated wild-type mice [53].

Butyrylcholinesterase (BChE) is an enzyme that can provide predictive value for the discovery and diagnosis of AD. Based on this, Liu and co-workers developed a near infrared fluorescence probe, Chy-1(**13**), to detect BChE activity [54]. Chromene-benzoindolum (Bhy) and chromeneindolum (Chy) were used as fluorophores, and cyclopropanecarboxylic acid chloride was used as an identifying motif. As the ideal linker, an ester group plays a critical role in the catalytic action of the probe toward BChE. **13** exhibited good biocompatibility, sensitivity (LOD: 0.12 ng/mL), and specificity for BChE detection. More importantly, **13** has also been successfully used to track BChE activity in AD mouse models. In conclusion, this probe is a powerful tool for the clinical diagnosis and treatment of cancer and neurodegenerative diseases.

Tau protein is a microtubule-associated protein that is highly expressed in neurons. However, the Tau protein in the brain of AD patients is abnormally hyperphosphorylated, and normal biological function is lost. Tau aggregation is also thought to be firmly linked to AD cognitive deficits. Nam et al. developed four quinoline-based fluorescent probes (**14**) for selective imaging of tau aggregation [55]. The selection of quinoline as a component of the probe was based on its potential and the excellent tau selectivity observed in previously reported THK compounds. The probe comprises an electron-rich moiety (donor region) with a dimethylaminophenyl/pyridinyl group and a relatively electron-deficient moiety (acceptor region) with a quinoline nucleus with or without a carbonyl group. The proposed mechanism for the “turn-on” fluorescence of the probe is an environment-sensitive, molecular rotor-like response. Compound **14** exhibited high selectivity and affinity ( $K_d = 16.6$  nM) for tau protein aggregates. In vitro staining of human AD brain tissue showed that the degree of colocalization of **14** and tau protein antibodies was higher than that of A $\beta$  fibrils. **14** was successfully used as a tau specific fluorescent imaging agent with low background interference. This work provides a new way to detect tau protein aggregation in AD.

#### 4. Parkinson's Disease

Parkinson's disease is a neurodegenerative disease characterized by clinical manifestations of motor retardation with quiescent tremor, tetania, or both [56]. Currently, there is no treatment that can slow or stop the progression of Parkinson's disease. Thus, numerous researchers have gained new insights into its pathogenesis via fluorescence imaging.

PD is closely related to oxidative stress, and ONOO<sup>-</sup> can cause cells to enter oxidative stress. Therefore, detection of ONOO<sup>-</sup> is helpful to explore the pathogenesis of PD [57]. Liu et al. synthesized a series of NIR probes, NIR-PNs (Figure 14, 15), to detect ONOO<sup>-</sup> in PD models [58]. A dicyanoisophorone with a donor (D)– $\pi$ –acceptor (A) structure was chosen for the fluorophore. The receptors, which were p-aminophenol molecules with substitutions such as 3-hydrogen/methoxy/methyl and 3,5-dimethyl groups, were selected as the ONOO<sup>-</sup> reactive site. **15** shows a fast response time (within 5 s) and is highly selective for ONOO<sup>-</sup> detection. **15** has been successfully applied to the imaging of ONOO<sup>-</sup> content in various PD models, including PC12 cells, drosophila, nematodes, and the mouse brain. This work advances our understanding of ONOO's biological involvement in Parkinson's disease.

Zhang et al. constructed a near-infrared ratio fluorescence probe (Figure 14, 16) for ONOO<sup>-</sup> in a PD model [59]. In **16**, a dicyanoisophorone derivative with the donor (D)-acceptor (A) structure is chosen as the NIR fluorophore, and a borate ester moiety is inserted into the probe as a specific recognition motif for ONOO<sup>-</sup> and as a weak electron-withdrawing group. Due to the breakage of the boronic acid ester group and the principle of ICT, **16** demonstrated a distinct ratiometric reaction towards ONOO<sup>-</sup>, resulting in red-shifted fluorescence. **16** exhibited a quantitative response to ONOO<sup>-</sup> (0–15  $\mu$ M) with a low detection limit (212 nM). By using fluorescent imaging, **16** can accurately monitor the change in ONOO<sup>-</sup> content in a rotenone-induced Parkinson's disease model. Therefore, **16** can be used as a potential tool to further investigate the biological and pathological effects of ONOO<sup>-</sup> in related diseases.

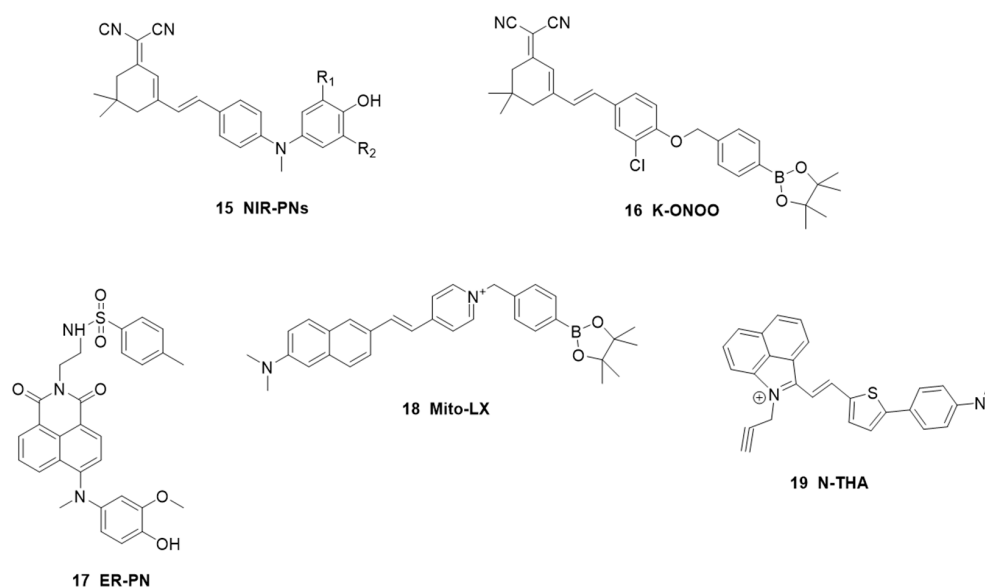


**Figure 14.** Chemical structure of the imaging probes for Parkinson's disease.

The endoplasmic reticulum (ER) is an important organelle involved in protein folding, cell signaling, and lipid metabolism [60].  $\text{ONOO}^-$  triggers an ER stress response that leads to neurodegeneration, including the death of dopaminergic neurons in the substantia nigra, a hallmark of PD [60]. Therefore, exploring endoplasmic reticulum stress is helpful to the treatment of PD. Xu et al. report a two-photon fluorescence probe, ER-PN (Figure 14, 17), for sensing and imaging  $\text{ONOO}^-$  in the endoplasmic reticulum in brain of PD mice [61]. In 17, 1,8-naphthalimide was used as a fluorophore, 4-amino-2-methoxyphenol (AP) was taken as an  $\text{ONOO}^-$  identifying group, and p-toluenesulfonamide served as an endoplasmic reticulum targeting group. Because of the PET effect, 17 exhibits weak fluorescence. When  $\text{ONOO}^-$  reacts with AP, the AP group is separated, restoring the fluorescence. 17 exerts excellent selectivity for  $\text{ONOO}^-$  detection. Furthermore, 17 has been successfully applied to  $\text{ONOO}^-$  imaging in PD models. Altogether, 17 has a potential application prospect in revealing the mechanism of endoplasmic reticulum stress and the occurrence and development of related diseases.

As the most active oxygen species in cells, hydrogen peroxide ( $\text{H}_2\text{O}_2$ ) is a key molecule affecting cellular oxidative stress [62]. Therefore, detection of  $\text{H}_2\text{O}_2$  can also contribute to exploring the pathogenesis of PD. Li et al. created a NIR fluorescent probe, NIR-HP1, for detecting  $\text{H}_2\text{O}_2$  in PD models [63]. The borate ester group was taken as the  $\text{H}_2\text{O}_2$  recognition group in NIR-HP1. NIR-HP1 emits green fluorescence owing to the incorporation of a borate ester group, which inhibits ESIPT-induced NIR emission. After reacting with  $\text{H}_2\text{O}_2$ , borate ester is removed and the phenol group is recovered, resulting in the ESIPT-induced NIR fluorescence emission (Figure 15). NIR-HP1 has the advantages of low toxicity, high sensitivity (LOD: 0.27  $\mu\text{M}$ ), and high selectivity for achieving ratio hydrogen peroxide imaging in PD models including living cells, zebrafish, and fruit flies. Thus, NIR-HP1 has application potential in PD research.

Mitochondria are the powerhouse of the cell and play a key role in generating neuronal energy. Mitochondrial dysfunction may lead to oxidative stress, which may affect PD. Therefore, mitochondria are closely related to PD [64]. Li and co-workers developed a mitochondrial targeted fluorescent probe, Mito-LX (Figure 14, 18), for dual imaging of viscosity and  $\text{H}_2\text{O}_2$  in PD models [65]. In 18, N, N-disubstituted units are utilized as strong electron-donating groups, and pyridine cations are utilized as electron-absorbing groups, forming a “donor–acceptor” molecular configuration conjugating with arylboronate groups as  $\text{H}_2\text{O}_2$  recognition groups. Pyridine cations could be capable of targeting mitochondria. As viscosity increases, intramolecular rotation is restricted, and intense red fluorescence emission is released. After the addition of  $\text{H}_2\text{O}_2$ , 18 will change from arylboric acid to

phenol, thus inhibiting the TICT effect and emitting orange fluorescence. **18** could directly and specifically image variations in hydrogen peroxide concentration and viscosity in the mitochondria of PD cells. Therefore, **18** is a useful tool for exploring  $\text{H}_2\text{O}_2$  and viscosity in the progression of Parkinson's disease.

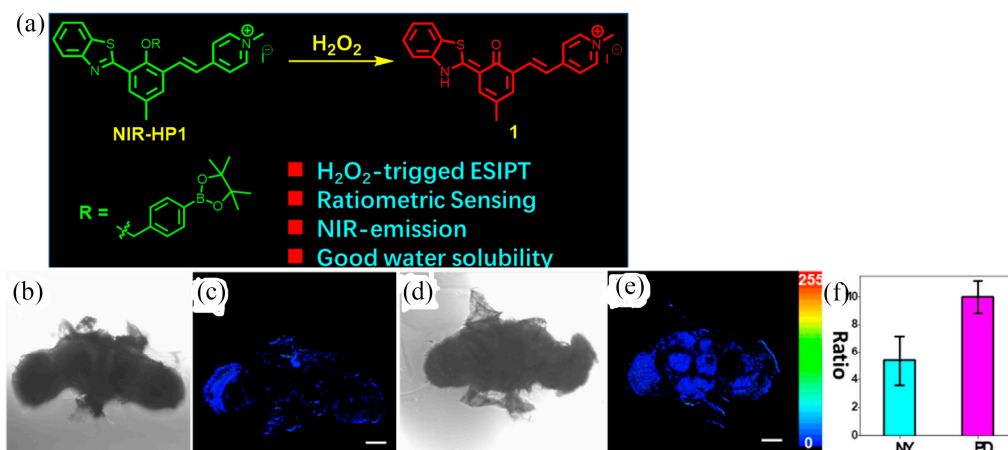


**Figure 15.** (a)  $\text{H}_2\text{O}_2$  sensing mode of NIR-HP1. (b) DIC of a wild-type (WT) Drosophila brain; (c) the ratio of red/green channel for WT; (d) DIC of a Parkinson's disease (PD) Drosophila brain; (e) the ratio of red/green channel for PD. (f) Ratio intensity profiles of Drosophila brain image panels: NY—wild type (WT) Drosophila brain; PD—Parkinson's disease (PD) Drosophila brain [63].

Zhu and colleagues developed a nanoprobe, TAT-Polyp-QL, which can detect accumulated iron and ROS simultaneously in the PD lesion area [66]. They designed a fluorescent molecule (Q1) containing quinoxalinone fluorophore and aromatic thioether, in which iron combines with a functional iron ligand (L1) to catalyze the formation of sulfoxide from aromatic sulfide, thus changing the fluorescence emission (Figure 16). HIV-1 trans-activating transcription factor (TAT) was introduced to promote the probe's crossing of the blood-brain barrier. Therefore, the probe achieves dual biomarker detection in the PD model, avoiding the false-positive results caused by traditional single biomarker detection.

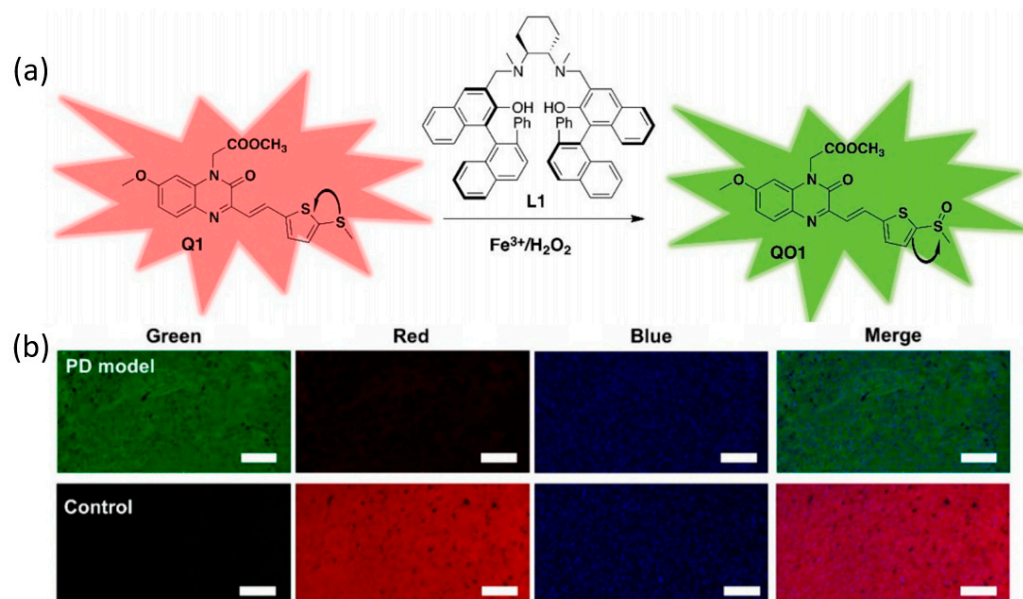


**Figure 16.** (a) Schematic representation of the oxidative process of Q1 upon meeting  $\text{H}_2\text{O}_2$  under the catalysis of  $\text{Fe}^{3+}$  and its ligand. (b) Confocal imaging of brain sections in a PD model and normal SD rats injected with TAT-Polyp-QL. The blue channel indicates a nucleus stained by DAPI [66].

Hypochlorous acid (HOCl) can induce an inflammatory response and increase the level of reactive oxygen species (ROS) in various cell types (including neurons), which is closely related to PD pathogenesis [67]. Chen and co-workers reported a fluorescent probe (NUU-1) for HOCl [68]. They chose phenothiazine as the HOCl recognition group and conjugated it with an aromatic amine to create the probe NUU-1 (Figure 17). NUU-1 emits weak fluorescence due to an efficient internal charge transfer (ICT) process caused by a strongly electrifying phenothiazine group. HOCl could oxidize sulfur atoms to sulphoxides, thereby reducing the ICT process and resulting in the recovery of fluorescence. NUU-1 showed rapid response (within 15 s), significant fluorescence enhancement (about 538 times), and excellent sensitivity (LOD: 25.8 nM) to HOCl. NUU-1 imaged HOCl in the brain of a mouse model and distinguished PD brain tissue from normal controls. Moreover, NUU-1 can be utilized to investigate the pathogenesis of HOCl-related diseases.

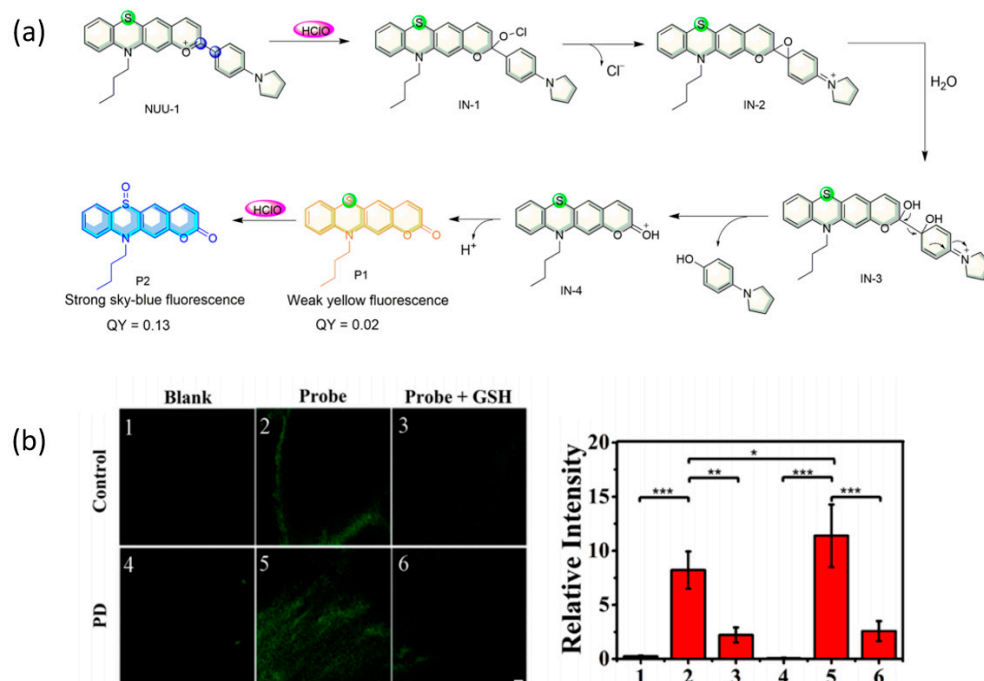


**Figure 17.** (a) Proposed reaction mechanism of NUU-1 toward HOCl. (b) Confocal fluorescence imaging of the probe NUU-1 in the substantia nigra region of the control and PD mouse brains. Brain slices were incubated with NUU-1 and average fluorescence intensities for panels (1–6). \*\*\*  $p < 0.005$ , \*\*  $p < 0.01$ , \*  $p < 0.05$  [68].

Yin et al. developed a dual-response fluorescent probe, N-THA (Figure 14, 19), for the detection of viscosity and hydrogen sulfide in mitochondria [69]. In 19, benzoindoles salt was conjugated with N, N-dimethyl-4(thiophen-2-yl)-aniline, which possessed potential for NIR emission. N-dimethyl-4(thiophen-2-yl)-aniline as a molecular rotor could respond to changes in viscosity with a 740 nm stronger fluorescent emission, whereas the C=C linker could sensitively respond to H<sub>2</sub>S with an increase in blue emission. The colocalization experiment proved the excellent mitochondrial targeting ability of 19 (Pearson colocalization coefficient 0.90). Furthermore, 19 can image viscosity changes in a Parkinson's disease model (PC-12 cells treated with glutamate). Therefore, this work provides a tool for the pathogenesis of Parkinson's disease related to viscosity and H<sub>2</sub>S.

## 5. Depression

Depression is the most common form of mood disorder. According to the World Health Organization, the number of people worldwide suffering from depression has exceeded 264 million [70]. Depression has become a major factor contributing to the global

burden of disease. However, the pathogenesis of depression is not clear, which greatly hampers the development of anti-depression treatments. Thus, there has been a lot of research into the molecular mechanisms of depression.

Oxidative stress in the brain is the excessive production of ROS, resulting in the damage of a large number of proteins, nucleic acids, and other biological macromolecules, thus leading to the occurrence and development of depression [71]. Cysteine (Cys), as a reducing amino acid, can regulate the level of oxidative stress in cells and then affect the occurrence and development of depression [72]. Our group developed a two-photon fluorescence probe, TCS (20), for detecting Cys in the brains of depressed mice [73]. In 20, the carbon–sulfur double bond is a key part of identifying Cys. Cys will form a five-membered ring with the carbon–sulfur double bond to restore coumarin’s push and pull electron effect, thus restoring its fluorescence. 20 was able to successfully image Cys in the mouse brain and found that Cys levels decreased with increasing levels of depressive behavior. This work provides a powerful tool for exploring the mechanisms of Cys-mediated-related diseases.

The superoxide anion radical ( $O_2^{\bullet-}$ ) is the first ROS produced and plays an important role in the occurrence and development of oxidative stress. We developed a two-photon fluorescent probe, TCP (Figure 18, 21), that can detect the superoxide anion radical ( $O_2^{\bullet-}$ ) in peroxisomes [74]. In 21, caffeic acid was selected as the  $O_2^{\bullet-}$  recognition group and fluorescence group, and SKL peptide was selected as the target group of peroxisomes.  $O_2^{\bullet-}$  can oxidize electron-donating catechol in caffeic acid residue to produce electron-absorbing catechol, thus changing the electron distribution of 21 and increasing its fluorescence. We found that overproduction of  $O_2^{\bullet-}$  by the peroxisome led to CAT inactivation. The inactivated CAT then leads to an overproduction of intracellular hydrogen peroxide, which further reduces TPH2 levels. The decrease in TPH2 led to abnormal function of 5-HT in the mouse brain, which eventually led to depression. This work provides evidence for the peroxisome  $O_2^{\bullet-}$ -mediated depression signaling pathway, which will help identify potential targets for depression treatment.

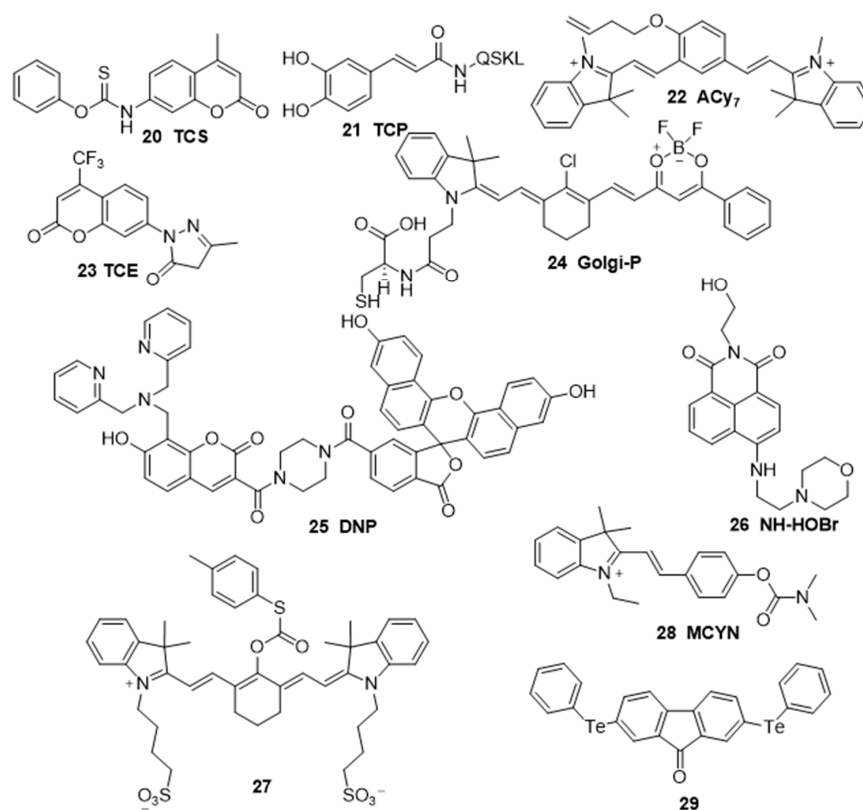


**Figure 18.** Chemical structure of probes for depression.

We developed Te-containing CDs (Figure 18, 29) for tracing native level changes in  $O_2^{\bullet-}$  within living systems [75]. Through the redox cycling between the Te and the Te=O, 29 has the ability to dynamically sense  $O_2^{\bullet-}$ . 29 exhibited reversibility, instantaneity, and the highest sensitivity (LOD~8.0 pM). Abdominal imaging of mice using 29 showed that  $O_2^{\bullet-}$  levels increased dramatically during intense exercise, irritability, and mild depression. In addition, dynamic brain imaging in a mouse model with mild depression showed higher levels of  $O_2^{\bullet-}$ . This work provides a novel strategy and an ideal imaging tool to reveal the health effects of acute exercise and mood changes at the ROS level.

Ozone ( $O_3$ ) can react with unsaturated fatty acids, resulting in the production of multiple ROS [76]. In turn, these ROS cause damage to cellular components such as DNA, proteins, and lipids, leading to a state of oxidative stress. We developed a near-infrared (NIR) fluorescent probe, ACy7 (Figure 18, 22), to directly observe  $O_3$  in the mouse brain [77]. Our probe uses a Cy7-like molecule as the precursor of the fluorophore and 3-butenyl as the recognition group. The terminal olefin of the 3-butenyl moiety can undergo a specific cycloaddition reaction with  $O_3$ , converting 22 into a quinone derivative, QCy7, and increasing the degree of conjugation. This leads to the emission of bright NIR fluorescence, enabling the detection of  $O_3$ . In situ imaging observations of  $O_3$  in brain tissue of depression-phenotypic mice were achieved, revealing an increase in  $O_3$  levels in depression-phenotypic mice. In addition,  $O_3$  in the brain induced depression in mice by producing excess IL-8. This work provides strong direct evidence for a positive association between  $O_3$  and depression and will help to more fully elucidate the pathogenesis of depression related to oxidative stress.

Hydroxyl radical ( $\cdot OH$ ), as the ROS with the strongest oxidizing ability, can cause serious damage to biomacromolecules and accelerate cell aging and death, thus leading to neurological diseases [78]. Exploring the relationship between changes in the concentration of  $\cdot OH$  in the living brain and depression will help deepen our understanding of the molecular mechanism of the occurrence and development of depression. We designed and synthesized a two-photon fluorescent probe TCE (Figure 19, 23) that visualized  $\cdot OH$  in the brain of mice with depression-like behavior in real time [79]. Trifluoromethyl acts as a strong electron-absorbing group, increasing the push and pull electron effect of coumarin, and also increasing its ability to cross the BBB.  $\cdot OH$  oxidizes TCE to form TCE-OH. TCE was used to detect increased  $\cdot OH$  content in the brain of mice with depression-like behavior, and the inactivation of SIRT1 by  $\cdot OH$  was the cause of the depressive phenotype. This work provides a useful tool for exploring  $\cdot OH$ -related diseases and helps to explore the molecular mechanism of depression.

Brain-derived neurotrophic factor (BDNF) is closely related to the occurrence and development of depression [80]. As the processing part of BDNF, the Golgi apparatus's microenvironment, including its polarity, may have a causal relationship with the level of BDNF [80]. Therefore, the change in polarity of the Golgi apparatus can effectively indicate the occurrence and development of depression. We construct a probe 24 that targets the Golgi apparatus and detects its polarity [81]. In 24, merocyanine is used as an electron donor, benzoyl difluoroboronate as an electron acceptor, and probe and solvent molecular dipole-dipole interactions in the polar environment lead to excited state energy. Therefore, 24 exhibits weak fluorescence emission in polar media and stronger fluorescence emission in non-polar media. L-cysteine was introduced to realize the Golgi apparatus targeting. By 24, we found significantly higher polarity in the brains of depressed phenotypic mice, and the increased polarity may be due to reduced BDNF synthesis. In conclusion, this study provides a new strategy for the accurate diagnosis of depression and a tool for exploring the occurrence and development mechanisms of depression.

The N-methyl-D-aspartic acid (NMDA) receptor is a subtype of the ionic glutamate receptor and an ion channel protein that plays an important role in the development of neurons and synaptic plasticity [82].  $Zn^{2+}$  and  $H^+$ , as regulatory binding partners of the NMDA receptor, are closely related to the activity of the NMDA receptor, and thus affect depression [83,84]. We developed a two-color fluorescent probe, DNP (Figure 18, 25), to simultaneously monitor  $Zn^{2+}$  and  $H^+$  in the brains of depressed mice. Fluorescein was

selected as a fluorophore, DPA (2,2'-dipicolylamine) as a  $Zn^{2+}$  recognition group, and naphthalene fluorescein as an  $H^+$  recognition group [85]. DPA quenches the fluorescence of coumarin through photoinduced electron transfer (PET). Encountering  $Zn^{2+}$ , PET would be blocked, causing bright blue fluorescence at 460 nm. With the addition of  $H^+$ , the red fluorescence at 680 nm was reduced due to the transformation of the naphtholuciferin group in the probe from an open quinone form to a closed spironolactone structure. By **25**, we detected increased levels of  $Zn^{2+}$  and  $H^+$  in PC12 cells under oxidative stress. In addition, both  $Zn^{2+}$  and pH were reduced in the brains of mice with depression-like behavior. The activity of the NMDA receptor may be related to the changes in  $Zn^{2+}$  and  $H^+$  content during depression. This work helps to reveal the relationship between  $Zn^{2+}$ ,  $H^+$ , and depression, and provides an effective tool for exploring the pathogenesis of depression.

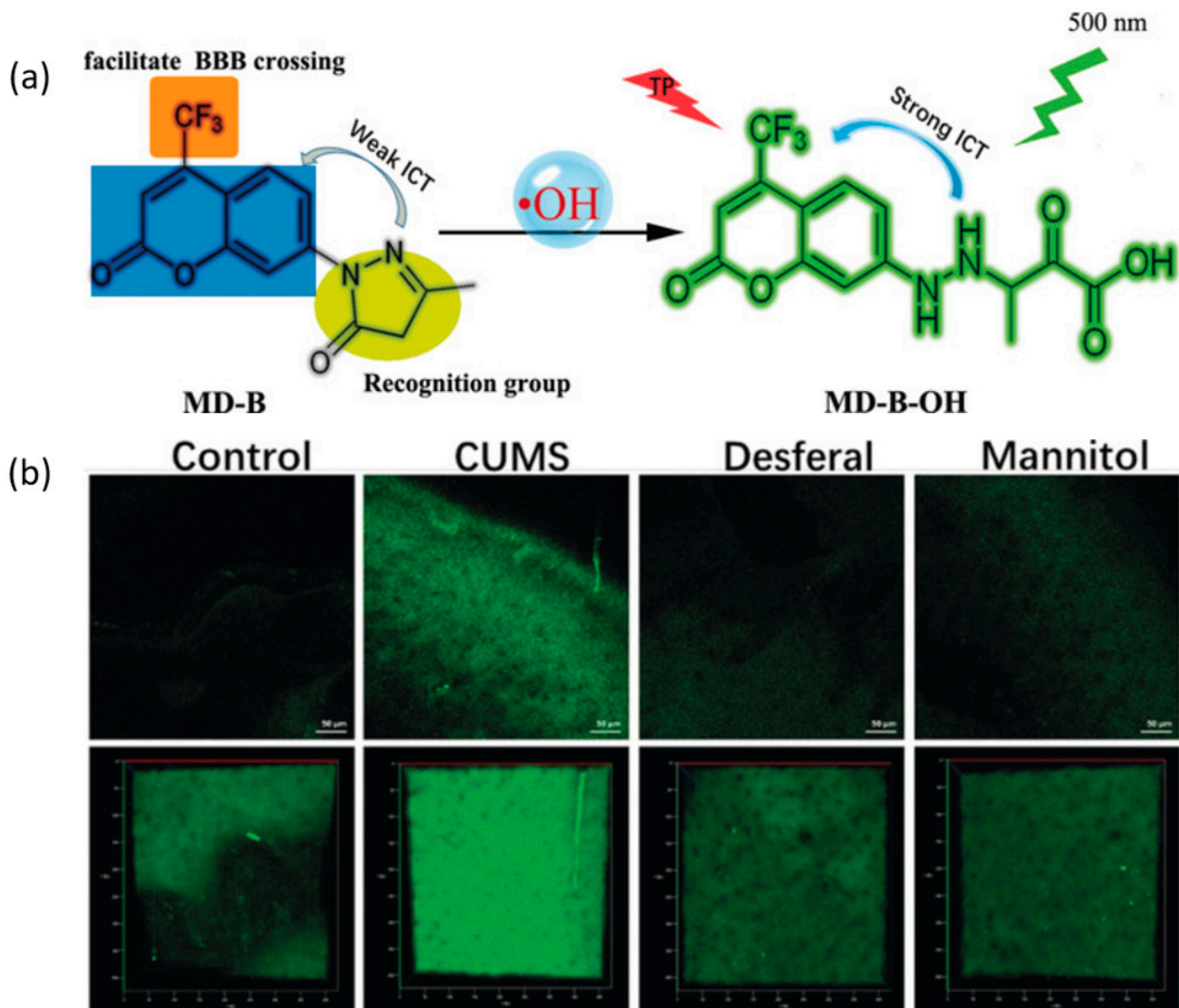


**Figure 19.** (a) The structure and luminescence mechanism of TCE. (b) In situ TP imaging of mice. Control: the mice without CUMS (chronic unpredictable mild stress). CUMS: the mice susceptible to CUMS. Desferal: The susceptible mice injected desferrioxamine (iron scavenger). Mannitol: The susceptible mice injected with mannitol ( $\bullet OH$  scavenger). Mannitol was used to scavenge hydroxyl radicals directly and Desferal was used to scavenge hydroxyl radicals by complexation with  $Fe^{2+}$  [79].

Hypobromic acid (HOBr), as a ROS, can damage proteins or lipids in cells and affect the normal physiological function of cells. We developed a two-photon fluorescent probe, NH-HOBr (Figure 18, **26**), for real-time visual monitoring of trace amounts of HOBr in

living systems [86]. 1, 8-Naphthylimide was selected as a two-photon fluorescence group, and N-(2-aminoethyl)-morpholine was selected as the lysosome target group and HOBr recognition group. **26** has the advantages of excellent selectivity, a fast response (5 s), and high sensitivity (LOD = 15 nM) to HOBr. **26** realized increased HOBr in inflammatory tissue, breast cancer tissue, and the brains of mice with depression.

Low levels of NE are often associated with the pathogenesis of depression [87]. Yin et al. developed a small molecule fluorescent probe (Figure 18, **27**) that can specifically detect norepinephrine (NE) using a “protect-deprotect” strategy [88]. **27** used cyanine as a fluorophore. NE will undergo a nucleophilic substitution reaction with carbon ester and release a fluorophore (Figure 20). **27** was able to detect norepinephrine specifically in complex biological systems, demonstrating the effect of antidepressant drugs on norepinephrine intervention. This strategy provides an effective tool for detecting the mechanism of norepinephrine and its associated diseases.

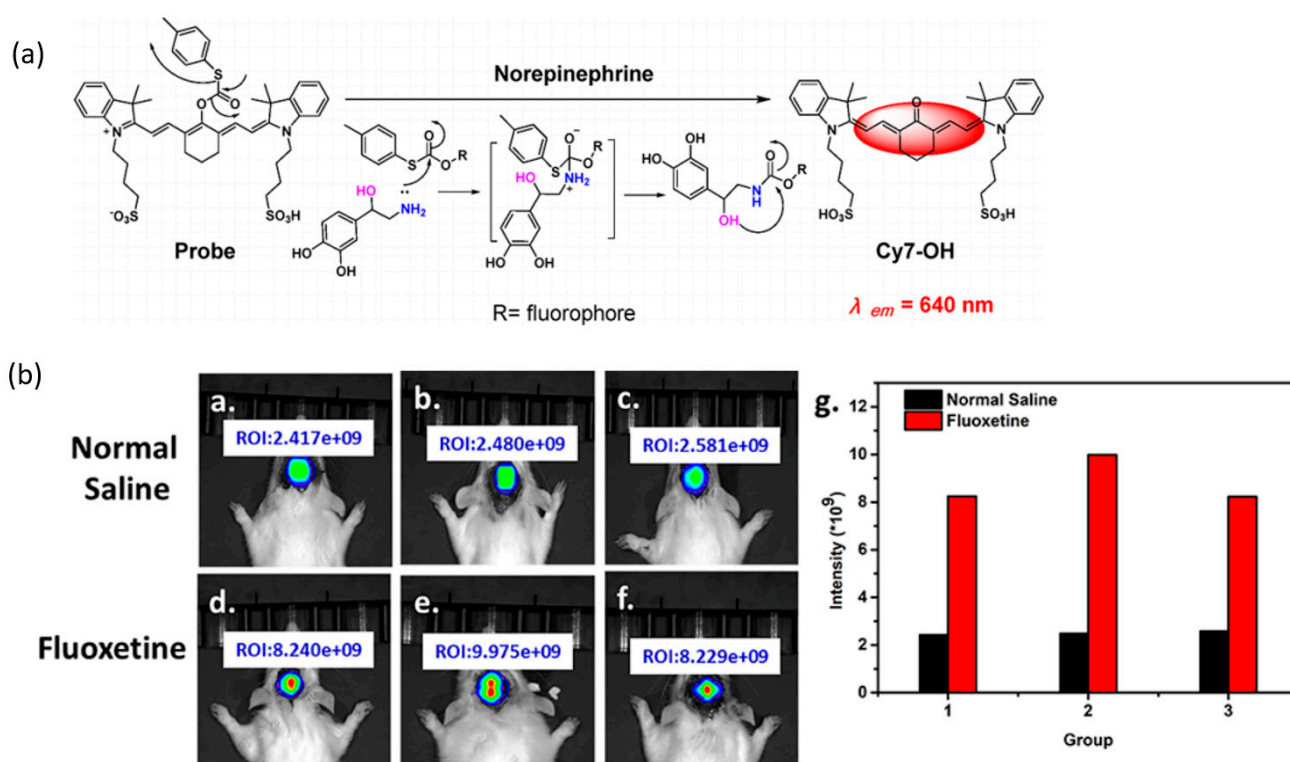


**Figure 20.** (a) Response mechanism of the probe with norepinephrine. (b): (a–c) In vivo imaging of rats intraperitoneally injected with saline; (d–f) in vivo imaging of rats intraperitoneally injected with fluoxetine. (g) Fluorescent intensity of ROIs in normal saline and fluoxetine-injected rats [86].

It has been shown that low levels of acetylcholinesterase may lead to depressive symptoms. In addition, acetylcholinesterase inhibitors have been found to be effective in alleviating depressive symptoms in some individuals [89]. We developed a two-photon fluorescence probe **28** to detect acetylcholinesterase (AChE) in the brains of depressed mice (Figure 18) [90]. Neostigmine, an inhibitor of AChE, was selected as the AChE recognition group and merocyanine as the fluorophore (Figure 21). The push-pull electron effect in MCYN is weakened by the carbon group, showing weak fluorescence. When combined with AChE, the ester bond is cleaved, the push-pull electron effect is enhanced, and the fluorescence is enhanced. Through MCYN, we found that AChE activity was positively correlated with depression-like degrees. In addition, we demonstrated that  $\text{O}_2^{\bullet-}$  can modulate AChE activity and lead to depressive symptoms. MCYN can be used as an effective tool to explore acetylcholinesterase-related diseases and provide important information for the treatment of depression.

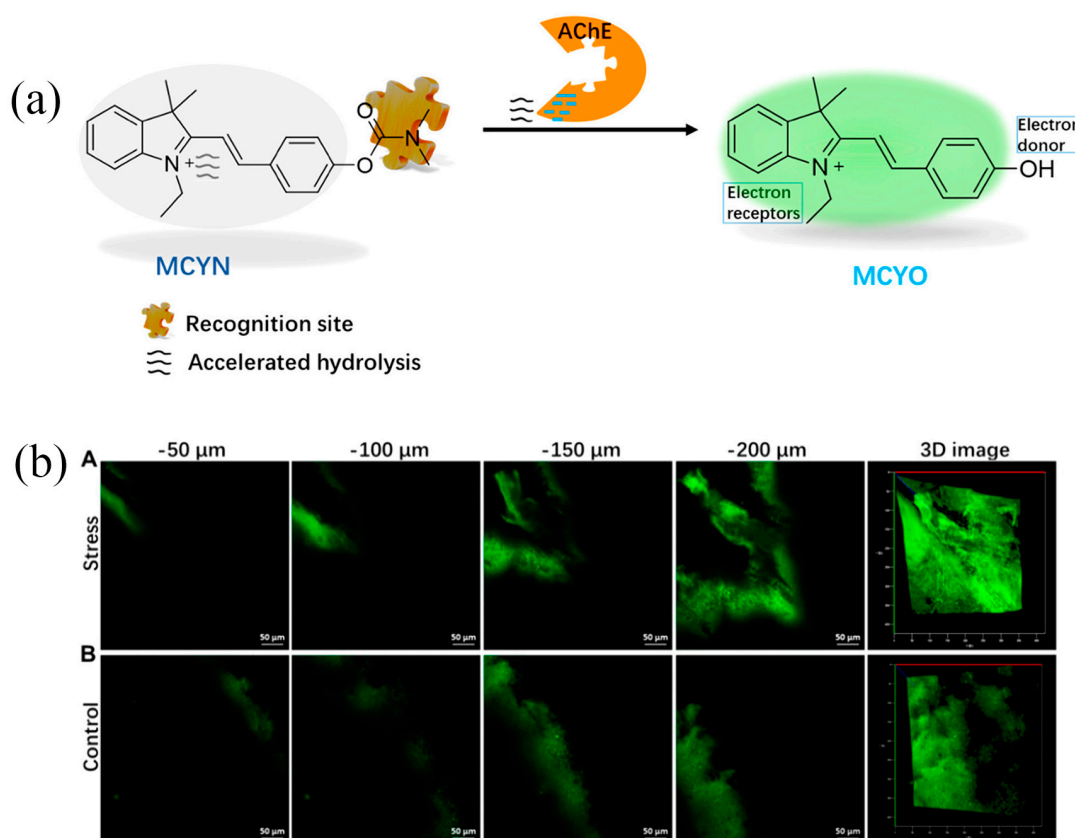


**Figure 21.** (a) Recognition mechanism of MCYN and structure of MCYO. (b) In situ TP fluorescence imaging in the brains of mice. (A) Stress: mice exposed to 14 consecutive days of chronic–restraint stress. (B) Control: mice not subjected to chronic–restraint stress [88].

We developed a nano-MOF nanoprobe with Zr(IV) and boric acid as active centers to detect phosphorylation levels [91]. In vivo imaging and two-photon imaging were used to study the relationship between glycosylation and phosphorylation in depressed mice. Imaging results showed that brain glycosylation and phosphorylation levels were significantly lower in depressed mice than in normal mice (Figure 22). On the one hand, this work provides an effective tool for studying glycosylation and phosphorylation, and on the other hand, it provides a new idea for revealing the pathogenesis of diseases.

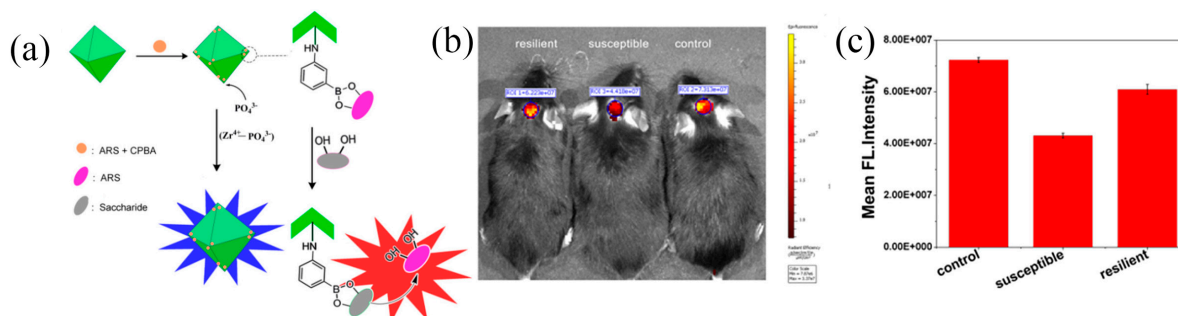


**Figure 22.** (a) Schematic illustration of the nanostructures of the probe. Visual images in the brains of mice. (b) Fluorescence imaging of glycosylation sites by MOF in resilient mice (left), susceptible mice (middle), and control mice (right). (c) Output of the fluorescence intensity of the images [89].

### 6. Schizophrenia

Schizophrenia is a chronic disease often manifested as a syndrome of different symptoms, involving sensory perception, thinking, emotion, and behavior in many aspects of

the disorder, as well as mental activity incoordination [92]. At present, its pathogenesis is still unclear. Many researchers have made significant contributions to the investigation of schizophrenia.

Through proteomic analysis, Yoshikawa et al. found that overproduction of hydrogen sulfide ( $\text{H}_2\text{S}$ ) may be a cause of schizophrenia [93]. Wang and co-workers developed three NIR fluorescent probes (Mind-SiR) based on the Si-rhodamine and hemicyanine structures for detecting  $\text{H}_2\text{S}$  [94]. They chose Si-rhodamine as fluorophores and introduced hemicyanine to adjust the solubility. Hemicyanine dyes can react with  $\text{H}_2\text{S}$  and change the solubility due to the positive charge (Figure 23). Mind-SiR has outstanding mitochondrial targeting, excellent brain uptake, and distinguished hydrogen sulfide selectivity. By Mind-SiR, the role of hydrogen sulfide in the pathogenesis and treatment of schizophrenia was revealed and provided direct evidence for abnormally elevated levels of hydrogen sulfide in the brains of schizophrenia mice. This work has the potential to evaluate the effects of drug therapy on schizophrenia.

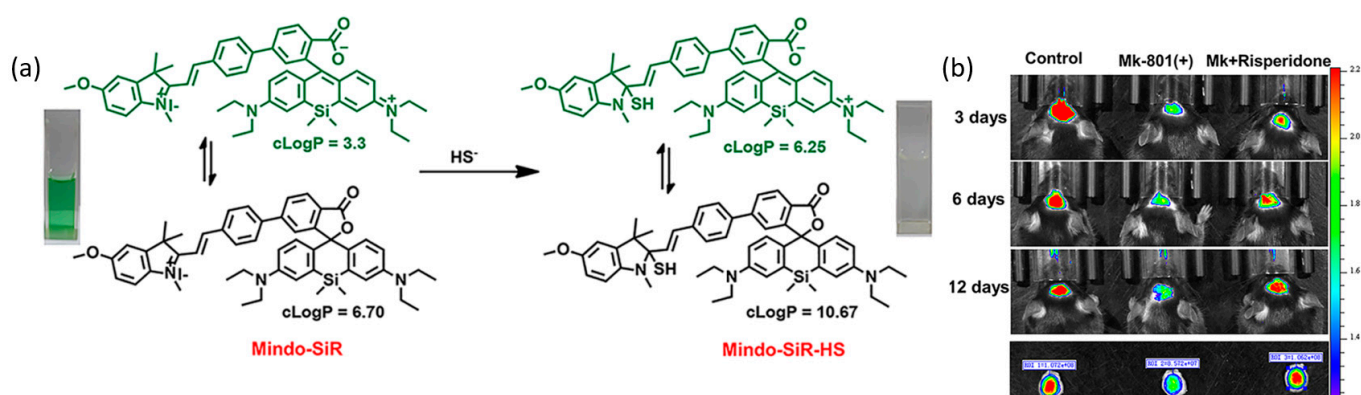


**Figure 23.** (a) Reaction mechanism of Mind-SiR and  $\text{HS}^-$ . (b) Mind-SiR was used to monitor the changes of the  $\text{H}_2\text{S}$  flux in the brain of SZ mice treated with risperidone at different times (3 days, 6 days, and 12 days) and fluorescence images of the dissected brains of the three mice (12 days) [92].

The D-amino acid oxidase (DAO) decomposes D-forms of amino acids to the corresponding  $\alpha$ -keto acids, hydrogen peroxide ( $\text{H}_2\text{O}_2$ ), and ammonia. DAO has been reportedly associated with several neuropsychiatric or neurological diseases, such as schizophrenia and amyotrophic lateral sclerosis (ALS) [95]. Fukushima et al. designed and synthesized a D-kynurenine (D-KYN) derivative, MeS-D-KYN, for detecting DAO activity [96]. The amino part of MeS-D-KYN was hydrolyzed to produce MeS-KYNA with blue fluorescence (Figure 24). MeS-D-KYN can be used for DAO fluorescence imaging in LLC-PK1 cells. MeS-D-KYN can be used as a molecular tool to explore DAO-related diseases, for DAO fluorescence imaging in LLC-PK1 cells, and as a molecular tool for exploring DAO-related diseases.

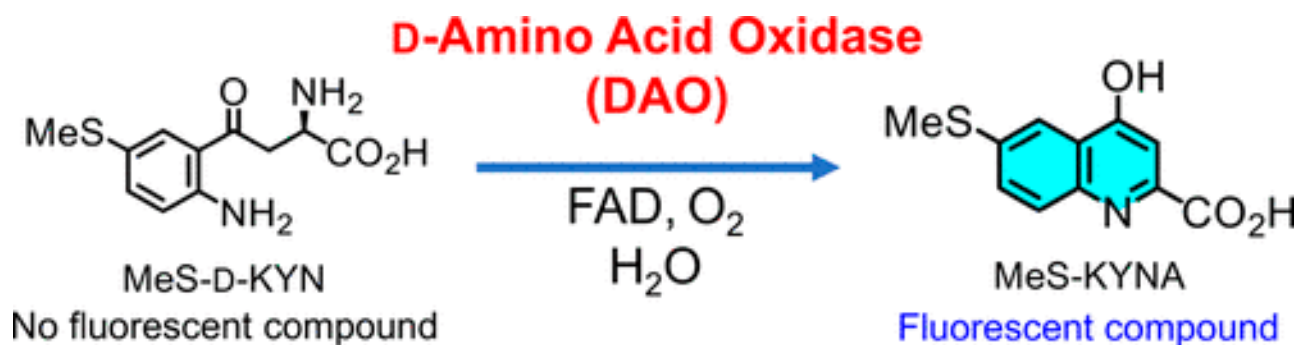


**Figure 24.** Reaction scheme of direct DAO activity determination method using MeS-D-KYN [94].

## 7. Conclusions and Prospects

The brain is the command center of the human body and the basis of mental activities. The occurrence of brain diseases seriously affects daily life and work. Therefore, it is important to be able to accurately diagnose brain diseases or understand the onset and progression of diseases. We reviewed the recent five years of small molecule fluorescence probes and nanofluorescence probes related to brain tumors, Alzheimer's disease, Parkinson's disease, depression, and schizophrenia (Table 1). Fluorescent probes have the advantages of high spatial and temporal resolution and are suitable for real-time in situ imaging detection in living cells or in vivo. To date, a number of fluorescent probes have been designed to image biomarkers of different brain diseases or to treat related diseases. The development of different fluorescent probes is expected to help diagnose disease-related biomarkers under different circumstances, explore the occurrence and development mechanisms of different diseases, and provide an effective tool for the diagnosis and treatment of related diseases.

**Table 1.** Category of fluorescent imaging agents for brain diseases.

Brain Disease	Probe Name	$\lambda$ ex/ $\lambda$ em (nm)	LOD	Bioactive Molecule	Biological Model	References
Brain tumors	m-PBTQ	900/950		N/A	C57BL/6 mice, ND2:SmoA1 mice	[27]
	TQFP-10 NPs	723/1020		N/A	subcutaneous U87 malignant (MG) tumor-bearing mice	[28]
	NaNdF4@NaLuF4/IR-808@DSPE-PEG5000 NP	808/1060,1340		N/A	U87-Luc cells, the tumor-bearing mice	[29]
	DCNPs	808/1525		N/A	U87 cells, orthotopic glioma bearing mice	[30]
	MFe <sub>3</sub> O <sub>4</sub> -Cy5.5	680/710		N/A	macrophages, C6 glioma cells	[31]
	CP NPs	980/1156	12.5 $\mu$ g/mL	N/A	Nude mice	[32]
	UIONPs	690~800/750~950		N/A	brain tumor-bearing mice, C6 cells	[33]
	RGD-RFP-LBT-Gd	584/607		N/A	tumor-bearing mice	[34]
	TB1	652/929		N/A	BALB/c nude mice	[35]
	B-AIE	280/340		N/A	C6-Luc cells, BALB/c nude mice	[36]
Alzheimer's disease	HA-AuNPs	355/438		hyaluronidase	HEK-293 cells	[37]
	CRANAD-2	640/820		A $\beta$ fibrils	arcA $\beta$ mice	[42]
	Gd(DOTA)-cyanine	465/600~760		A $\beta$	SH-SY5Y cells, 5XFAD-Tg mice, double transgenic (APP/PS1) model mice	[43]
	Rho4-Cu	540/594		A $\beta$ 42	APP/PS1 mice	[44]
	Eth-BF	808/1015		A $\beta$ oligomers	HaCat, HeLa and bEnd.3 cells, APP/PS1 Tg mice	[45]
	RB-CDs	430/582~675	0.5 pM	A $\beta$ peptide	SH-SY5 cells	[46]
	PTAD-3	453/580		A $\beta$ aggregates	HeLa and U87 cells, APP/PS1 transgenic mice	[47]
	CAQ	565/635		A $\beta$ aggregates	Nematode AD model, 5 $\times$ FAD-transgenic mice	[48]
	BTNPO	340/418		peroxynitrite	PC12 cells, APP/PS1 double transgenic mice	[49]
	Rd-DPA3	602/702		peroxynitrite	PC12 cells, AD mouse	[51]
	Golgi-NO	560/589		nitric oxide	HepG2 and SH-SY5Y cells, SH-SH5Y cells	[52]
	TM-IONP	808/1000~1700	210 nM	methylglyoxal	AD mouse	[53]
	Chy-1	670/715	0.12 ng/mL	butyrylcholinesterase	SH-SY5Y cells, HepG2 and 293T cells, AD model transgenic mice	[54]
	Q-tau 4	424/637		tau	Human Neuron Cell Line (SHSY-5Y)	[55]

Table 1. Cont.

Brain Disease	Probe Name	$\lambda$ ex/ $\lambda$ em (nm)	LOD	Bioactive Molecule	Biological Model	References
Parkinson's disease	NIR-PN1	510 /670	4.59 nM	peroxynitrite	PC12 and SH-SY5Y cells, parkin null Drosophila, WLZ3 C. elegans	[58]
	K-ONOO	405/570	212 nM	peroxynitrite	HeLa cells, zebrafish	[59]
	ER-PN	488/540	8.3 nM	peroxynitrite	PC12 cells, WLZ3 elegans	[61]
	NIR-HP1	395/500,650	0.27 $\mu$ M	hydrogen peroxide	living cells, zebrafish and drosophila	[63]
	Mito-LX	380/585		hydrogen peroxide/viscosity	HepG2 cells, zebrafish and drosophila	[65]
	TAT-Polyp-QL	458/600	0.3832 $\mu$ M	iron and reactive oxygen	PC12 cells, SD rats	[66]
	NUU-1	438/503	25.8 nM	hypochlorous acid	SH-SY5Y cells, drosophila, PD mouse	[68]
	N-THA	385/516		viscosity and hydrogen sulfide	HeLa cells, PD mouse	[69]
Depression	TCS	340/443	0.16 $\mu$ M	cysteine	PC12 cells, C57BL/6J mice	[73]
	TCP	370/495	21.5 nM	superoxide anion radical	PC12 cells, C57BL/6J mice	[74]
	Te-CDs	380/440	8.0 pM	superoxide anion radical	HepG2 cells, macrophages, Hela cells and lung cancer cells, BalB/C mice	[75]
	ACy7	570/690	10 nM	ozone	RAW 264.7 Macrophages, CUMS mouse model	[77]
	TCE	370/500	2.4 $\mu$ M	hydroxyl radical	PC12 cells, PC12 cells, C57BL/6J mice	[79]
	Golgi-P	700/780		brain-derived neurotrophic factor	PC12 cells, PC12 cells, C57BL/6J mice	[81]
	DNP	390/460	0.32 $\mu$ M	Zn <sup>2+</sup> and H <sup>+</sup>	PC12 cells, C57 mouse	[85]
	NH-HOBr	400/505	15 nM	hypobromic acid	PC12 cells, RAW 264.7 Macrophages, zebrafish, mice	[86]
	Cy7-OH	550/640		norepinephrine	PC12 cells, HepG2 cells, SD rats	[88]
	MCYN	520/560	0.36 $\mu$ M	acetylcholinesterase	PC12 cells, mice	[90]
	UIO-66-NH2	425/610		phosphorylation	HL-7702 cells, mice	[91]
	Schizophrenia	Mindo-SiR	650/680	0.45 $\mu$ M	hydrogen sulfide	bEnd.3 cells, schizophrenia mouse
MeS-D-KYN		364/450	18.2 mU/mL	D-amino acid oxidase	LLC-PK1 cells	[96]

However, due to the complex physiological environment of cells in vivo, the construction of fluorescence imaging tools has high requirements. There have been exciting advances in the development of existing imaging tools, but there are still some unresolved challenges to overcome. First, most fluorescent probes are single-color fluorescent probes for single biomarkers. In the physiological and pathological processes of organisms, multiple components often play a role together, so it is difficult to observe the synergistic changes of multiple related substances with fluorescent probes only targeting a single component. It is easy to interfere with the diagnosis of other diseases and affect the accuracy of the diagnosis. Secondly, many fluorescent probes are difficult to accurately reach and stay in the brain. On the one hand, the existence of the blood–brain barrier protects the brain from the invasion of harmful substances; on the other hand, it also prevents the intake of partial fluorescent probes, thus affecting its further development. Finally, the thickness of brain tissue imposes greater challenges for fluorescence imaging of the brain, especially the human brain, which has an average size of  $140 \times 167 \times 93$  mm [97]. Currently, the penetration depth of two-photon or three-photon imaging can exceed the mm level, which to some extent overcomes the obstacle of penetration. NIR II imaging could reach a depth of up to 1cm, which has been clinically used in gastrointestinal endoscopy [98]. Moreover, utilizing fluorescent probes, fluorescence imaging technology offers a promising method for in vitro diagnosis of human brain diseases. However, real-time in situ fluorescence

imaging of the human brain is still insufficient. Therefore, it is essential to advance the development of more effective two-photon, three-photon, or NIR-II fluorescent probes.

In conclusion, the development of new fluorescent probes for detecting brain diseases will still be an important research topic in the future development frontier of fluorescence imaging, which will provide important new materials and new methods for revealing the occurrence and development process of brain diseases as well as diagnosis and treatment. We hope that the current summary of some of the brain disease imaging tools will lay the foundation for future advances.

**Author Contributions:** F.C.: literature review, manuscript preparation, writing—original draft. X.W.: literature review, manuscript preparation, writing—original draft. X.Z.: literature review, manuscript preparation. P.L.: review and edit. B.T.: review and edit. All authors have read and agreed to the published version of the manuscript.

**Funding:** This work was supported by the National Natural Science Foundation of China (22134004, 21927811, 22074083), the Key Research and Development Program of Shandong Province (2018YFJH0502), and the National Science Foundation of Shandong Province of China (ZR2020ZD17).

**Institutional Review Board Statement:** Not applicable.

**Informed Consent Statement:** Not applicable.

**Data Availability Statement:** Not applicable.

**Conflicts of Interest:** The authors declare no conflict of interest.

## References

- McEwen, B.S. The Brain on Stress: Toward an Integrative Approach to Brain, Body, and Behavior. *Perspect. Psychol. Sci.* **2013**, *8*, 673–675. [[CrossRef](#)] [[PubMed](#)]
- Fornito, A.; Bullmore, E.T. Connectomics: A new paradigm for understanding brain disease. *Eur. Neuropsychopharmacol.* **2015**, *25*, 733–748. [[CrossRef](#)] [[PubMed](#)]
- Butterfield, D.A.; Perluigi, M.; Sultana, R. Oxidative stress in Alzheimer’s disease brain: New insights from redox proteomics. *Eur. J. Pharmacol.* **2006**, *545*, 39–50. [[CrossRef](#)] [[PubMed](#)]
- Butterfield, D.A. Proteomics: A new approach to investigate oxidative stress in Alzheimer’s disease brain. *Brain Res. Brain Res. Rev.* **2004**, *1000*, 1–7. [[CrossRef](#)]
- Harris, A.N.; Beatty, S.S.; Estrada, A.H.; Winter, B.; Bohannon, M.; Sosa, I.; Hanscom, J.; Mainville, C.A.; Gallagher, A.E. Investigation of an N-Terminal Prohormone of Brain Natriuretic Peptide Point-of-Care ELISA in Clinically Normal Cats and Cats With Cardiac Disease. *J. Vet. Intern. Med.* **2017**, *31*, 994–999. [[CrossRef](#)]
- Fauss, D.; Motter, R.; Dofiles, L.; Rodrigues, M.A.V.; You, M.; Diep, L.; Yang, Y.; Seto, P.; Tanaka, K.; Baker, J.; et al. Development of an enzyme-linked immunosorbent assay (ELISA) to measure the level of tyrosine hydroxylase protein in brain tissue from Parkinson’s disease models. *J. Neurosci. Methods* **2013**, *215*, 245–257. [[CrossRef](#)]
- Sizova, D.; Charbaut, E.; Delalande, F.; Poirier, F.; High, A.A.; Parker, F.; Van Dorsselaer, A.; Duchesne, M.; Diu-Hercend, A. Proteomic analysis of brain tissue from an Alzheimer’s disease mouse model by two-dimensional difference gel electrophoresis. *Neurobiol. Aging* **2007**, *28*, 357–370. [[CrossRef](#)]
- Yu, C.H.; Song, G.S.; Yhee, J.Y.; Kim, J.H.; Im, K.S.; Nho, W.G.; Lee, J.H.; Sur, J.H. Histopathological and Immunohistochemical Comparison of the Brain of Human Patients with Alzheimer’s Disease and the Brain of Aged Dogs with Cognitive Dysfunction. *J. Comp. Pathol.* **2011**, *145*, 45–58. [[CrossRef](#)]
- Ibanez, F.G.; Picard, K.; Bordeleau, M.; Sharma, K.; Bisht, K.; Tremblay, M.È. Immunofluorescence Staining Using IBA1 and TMEM119 for Microglial Density, Morphology and Peripheral Myeloid Cell Infiltration Analysis in Mouse Brain. *J. Visualized Exp.* **2019**, *152*, e60510. [[CrossRef](#)]
- Wang, G.; Achim, C.L.; Hamilton, R.L.; Wiley, C.A.; Soontornniyomkij, V. Tyramide Signal Amplification Method in Multiple-Label Immunofluorescence Confocal Microscopy. *Methods* **1999**, *18*, 459–464. [[CrossRef](#)]
- Iwaki, T.; Kume-Iwaki, A.; Liem, R.K.H.; Goldman, J.E.  $\alpha$ B-crystallin is expressed in non-lenticular tissues and accumulates in Alexander’s disease brain. *Cell* **1989**, *57*, 71–78. [[CrossRef](#)]
- Ferrer, I.; Santpere, G.; Arzberger, T.; Bell, J.; Blanco, R.; Boluda, S.; Budka, H.; Carmona, M.; Giaccone, G.; Krebs, B.; et al. Brain Protein Preservation Largely Depends on the Postmortem Storage Temperature: Implications for Study of Proteins in Human Neurologic Diseases and Management of Brain Banks: A BrainNet Europe Study. *J. Neuropathol. Exp. Neurol.* **2007**, *66*, 35–46. [[CrossRef](#)] [[PubMed](#)]
- Bles, M.; Haynes, J.-D. Detecting concealed information using brain-imaging technology. *Neurocase* **2008**, *14*, 82–92. [[CrossRef](#)] [[PubMed](#)]
- Garcia-Alloza, M.; Bacskai, B.J. Techniques for brain imaging in vivo. *Neuro Mol. Med.* **2004**, *6*, 65–78. [[CrossRef](#)] [[PubMed](#)]

15. Bowman, F.D. Brain Imaging Analysis. *Annu. Rev. Stat. Appl.* **2014**, *1*, 61–85. [[CrossRef](#)] [[PubMed](#)]
16. Li, W.; Yin, S.; Shen, Y.; Li, H.; Yuan, L.; Zhang, X.B. Molecular Engineering of pH-Responsive NIR Oxazine Assemblies for Evoking Tumor Ferroptosis via Triggering Lysosomal Dysfunction. *J. Am. Chem. Soc.* **2023**, *145*, 3736–3747. [[CrossRef](#)]
17. Rao, J.; Dragulescu-Andrasi, A.; Yao, H. Fluorescence imaging in vivo: Recent advances. *Curr. Opin. Biotechnol.* **2007**, *18*, 17–25. [[CrossRef](#)]
18. Laissue, P.P.; Alghamdi, R.A.; Tomancak, P.; Reynaud, E.G.; Shroff, H. Assessing phototoxicity in live fluorescence imaging. *Nat. Methods* **2017**, *14*, 657–661. [[CrossRef](#)]
19. Liu, J.; Zhang, W.; Zhou, C.; Li, M.; Wang, X.; Zhang, W.; Liu, Z.; Wu, L.; James, T.D.; Li, P.; et al. Precision Navigation of Hepatic Ischemia–Reperfusion Injury Guided by Lysosomal Viscosity-Activatable NIR-II Fluorescence. *J. Am. Chem. Soc.* **2022**, *144*, 13586–13599. [[CrossRef](#)]
20. Ren, T.B.; Wang, Z.Y.; Xiang, Z.; Lu, P.; Lai, H.H.; Yuan, L.; Zhang, X.B.; Tan, W. A General Strategy for Development of Activatable NIR-II Fluorescent Probes for In Vivo High-Contrast Bioimaging. *Angew. Chem. Int. Ed.* **2021**, *60*, 800–805. [[CrossRef](#)]
21. Mao, L.; Han, Y.; Zhang, Q.W.; Tian, Y. Two-photon fluorescence imaging and specifically biosensing of norepinephrine on a 100-ms timescale. *Nat. Commun.* **2023**, *14*, 1419. [[CrossRef](#)] [[PubMed](#)]
22. Zhao, Y.; Kim, H.S.; Zou, X.; Huang, L.; Liang, X.; Li, Z.; Kim, J.S.; Lin, W. Harnessing Dual-Fluorescence Lifetime Probes to Validate Regulatory Mechanisms of Organelle Interactions. *J. Am. Chem. Soc.* **2022**, *144*, 20854–20865. [[CrossRef](#)]
23. Wu, X.; Wang, R.; Qi, S.; Kwon, N.; Han, J.; Kim, H.; Li, H.; Yu, F.; Yoon, J. Rational Design of a Highly Selective Near-Infrared Two-Photon Fluorogenic Probe for Imaging Orthotopic Hepatocellular Carcinoma Chemotherapy. *Angew. Chem. Int. Ed.* **2021**, *60*, 15418–15425. [[CrossRef](#)]
24. Weller, M.; Wick, W.; Aldape, K.; Brada, M.; Berger, M.; Pfister, S.M.; Nishikawa, R.; Rosenthal, M.; Wen, P.Y.; Stupp, R.; et al. Glioma. *Nat. Rev. Dis. Prim.* **2015**, *1*, 15017. [[CrossRef](#)]
25. Hong, G.; Diao, S.; Chang, J.; Antaris, A.L.; Chen, C.; Zhang, B.; Zhao, S.; Atochin, D.N.; Huang, P.L.; Andreasson, K.I.; et al. Through-skull fluorescence imaging of the brain in a new near-infrared window. *Nat. Photonics* **2014**, *8*, 723–730. [[CrossRef](#)]
26. Frangioni, J.V. In vivo near-infrared fluorescence imaging. *Curr. Opin. Chem. Biol.* **2003**, *7*, 626–634. [[CrossRef](#)]
27. Liu, Y.; Liu, J.; Chen, D.; Wang, X.; Zhang, Z.; Yang, Y.; Jiang, L.; Qi, W.; Ye, Z.; He, S.; et al. Fluorination Enhances NIR-II Fluorescence of Polymer Dots for Quantitative Brain Tumor Imaging. *Angew. Chem. Int. Ed.* **2020**, *59*, 21049–21057. [[CrossRef](#)]
28. Chen, S.; Miao, H.; Jiang, X.; Sun, P.; Fan, Q.; Huang, W. Starlike polymer brush-based ultrasmall nanoparticles with simultaneously improved NIR-II fluorescence and blood circulation for efficient orthotopic glioblastoma imaging. *Biomaterials* **2021**, *275*, 120916. [[CrossRef](#)]
29. Liu, Z.; Ren, F.; Zhang, H.; Yuan, Q.; Jiang, Z.; Liu, H.; Sun, Q.; Li, Z. Boosting often overlooked long wavelength emissions of rare-earth nanoparticles for NIR-II fluorescence imaging of orthotopic glioblastoma. *Biomaterials* **2019**, *219*, 119364. [[CrossRef](#)] [[PubMed](#)]
30. Ren, F.; Liu, H.; Zhang, H.; Jiang, Z.; Xia, B.; Genevois, C.; He, T.; Allix, M.; Sun, Q.; Li, Z.; et al. Engineering NIR-IIb fluorescence of Er-based lanthanide nanoparticles for through-skull targeted imaging and imaging-guided surgery of orthotopic glioma. *Nano Today* **2020**, *34*, 100905. [[CrossRef](#)]
31. Wang, S.; Shen, H.; Mao, Q.; Tao, Q.; Yuan, G.; Zeng, L.; Chen, Z.; Zhang, Y.; Cheng, L.; Zhang, J.; et al. Macrophage-Mediated Porous Magnetic Nanoparticles for Multimodal Imaging and Postoperative Photothermal Therapy of Gliomas. *ACS Appl. Mater. Interfaces* **2021**, *13*, 56825–56837. [[CrossRef](#)]
32. Guo, B.; Feng, Z.; Hu, D.; Xu, S.; Middha, E.; Pan, Y.; Liu, C.; Zheng, H.; Qian, J.; Sheng, Z.; et al. Precise Deciphering of Brain Vasculatures and Microscopic Tumors with Dual NIR-II Fluorescence and Photoacoustic Imaging. *Adv. Mater.* **2019**, *31*, e1902504. [[CrossRef](#)]
33. Duan, Y.; Hu, D.; Guo, B.; Shi, Q.; Wu, M.; Xu, S.; Kenry; Liu, X.; Jiang, J.; Sheng, Z.; et al. Nanostructural Control Enables Optimized Photoacoustic–Fluorescence–Magnetic Resonance Multimodal Imaging and Photothermal Therapy of Brain Tumor. *Adv. Funct. Mater.* **2019**, *30*, 1907077. [[CrossRef](#)]
34. Zhao, H.; Zhao, H.; Jiao, Y.; Zhu, Y.; Liu, C.; Li, F.; Wang, Y.; Gu, Z.; Yang, D. Biosynthetic molecular imaging probe for tumor-targeted dual-modal fluorescence/magnetic resonance imaging. *Biomaterials* **2020**, *256*, 120220. [[CrossRef](#)] [[PubMed](#)]
35. Sheng, Z.; Guo, B.; Hu, D.; Xu, S.; Wu, W.; Liew, W.H.; Yao, K.; Jiang, J.; Liu, C.; Zheng, H.; et al. Bright Aggregation-Induced-Emission Dots for Targeted Synergetic NIR-II Fluorescence and NIR-I Photoacoustic Imaging of Orthotopic Brain Tumors. *Adv. Mater.* **2018**, *30*, e1800766. [[CrossRef](#)] [[PubMed](#)]
36. Gao, D.; Li, Y.; Wu, Y.; Liu, Y.; Hu, D.; Liang, S.; Liao, J.; Pan, M.; Zhang, P.; Li, K.; et al. Albumin-Consolidated AIEgens for Boosting Glioma and Cerebrovascular NIR-II Fluorescence Imaging. *ACS Appl. Mater. Interfaces* **2023**, *15*, 3–13. [[CrossRef](#)]
37. Liu, J.W.; Wang, Y.M.; Zhang, C.H.; Duan, L.Y.; Li, Z.; Yu, R.Q.; Jiang, J.H. Tumor-Targeted Graphitic Carbon Nitride Nanoassembly for Activatable Two-Photon Fluorescence Imaging. *Anal. Chem.* **2018**, *90*, 4649–4656. [[CrossRef](#)]
38. Scheltens, P.; Blennow, K.; Breteler, M.M.B.; de Strooper, B.; Frisoni, G.B.; Salloway, S.; Van der Flier, W.M. Alzheimer’s disease. *Lancet* **2016**, *388*, 505–517. [[CrossRef](#)]
39. Chasseigneaux, S.; Allinquant, B. Functions of A $\beta$ , sAPP $\alpha$  and sAPP $\beta$ : Similarities and differences. *J. Neurochem.* **2012**, *120*, 99–108. [[CrossRef](#)]
40. Cavallucci, V.; D’Amelio, M.; Cecconi, F. A $\beta$  Toxicity in Alzheimer’s Disease. *Mol. Neurobiol.* **2012**, *45*, 366–378. [[CrossRef](#)]

41. Tanzi, R.E.; Moir, R.D.; Wagner, S.L. Clearance of Alzheimer's A $\beta$  Peptide: The Many Roads to Perdition. *Neuron* **2004**, *43*, 605–608. [[CrossRef](#)] [[PubMed](#)]
42. Ni, R.; Villosio, A.; Dean-Ben, X.L.; Chen, Z.; Vaas, M.; Stavarakis, S.; Shi, G.; de Mello, A.; Ran, C.; Razansky, D.; et al. In-vitro and in-vivo characterization of CRANAD-2 for multi-spectral optoacoustic tomography and fluorescence imaging of amyloid-beta deposits in Alzheimer mice. *Photoacoustics* **2021**, *23*, 100285. [[CrossRef](#)]
43. Wang, X.; Chan, H.N.; Desbois, N.; Gros, C.P.; Bolze, F.; Li, Y.; Li, H.W.; Wong, M.S. Multimodal Theranostic Cyanine-Conjugated Gadolinium(III) Complex for In Vivo Imaging of Amyloid-beta in an Alzheimer's Disease Mouse Model. *ACS Appl. Mater. Interfaces* **2021**, *13*, 18525–18532. [[CrossRef](#)] [[PubMed](#)]
44. Xiang, J.; Xiang, C.; Zhou, L.; Sun, M.; Feng, L.; Liu, C.; Cai, L.; Gong, P. Rational Design, Synthesis of Fluorescence Probes for Quantitative Detection of Amyloid-beta in Alzheimer's Disease Based on Rhodamine-Metal Complex. *Anal. Chem.* **2022**, *94*, 11791–11797. [[CrossRef](#)] [[PubMed](#)]
45. Li, H.; Wang, J.; Li, Y.; Chen, X.; Zhang, W.; Zhao, Y.; Liu, G.; Pan, J. Detection of A $\beta$  oligomers in early Alzheimer's disease diagnose by in vivo NIR-II fluorescence imaging. *Sens. Actuators B Chem.* **2022**, *358*, 131481. [[CrossRef](#)]
46. Hamd-Ghadareh, S.; Salimi, A.; Parsa, S.; Mowla, S.J. Development of three-dimensional semi-solid hydrogel matrices for ratiometric fluorescence sensing of Amyloid beta peptide and imaging in SH-SY5 cells: Improvement of point of care diagnosis of Alzheimer's disease biomarker. *Biosens Bioelectron.* **2022**, *199*, 113895. [[CrossRef](#)] [[PubMed](#)]
47. Gu, Y.; Ding, Z.; Zheng, C.; Xu, Y.; Liu, T.; Mao, C.; Ran, C.; Yang, J.; Wang, P. Light-controlled fluorescent probes for precisely monitoring brain amyloid- $\beta$  aggregates in Alzheimer's disease. *Chem. Eng. J.* **2022**, *446*, 137385. [[CrossRef](#)]
48. Wu, J.; Shao, C.; Ye, X.; Di, X.; Li, D.; Zhao, H.; Zhang, B.; Chen, G.; Liu, H.K.; Qian, Y. InVivo Brain Imaging of Amyloid-beta Aggregates in Alzheimer's Disease with a Near-Infrared Fluorescent Probe. *ACS Sens.* **2021**, *6*, 863–870. [[CrossRef](#)]
49. Koppal, T.; Drake, J.; Yatin, S.; Jordan, B.; Varadarajan, S.; Bettenhausen, L.; Butterfield, D.A. Peroxynitrite-Induced Alterations in Synaptosomal Membrane Proteins. *J. Neurochem.* **1999**, *72*, 310–317. [[CrossRef](#)]
50. Xie, X.; Liu, G.; Niu, Y.; Xu, C.; Li, Y.; Zhang, J.; Jiao, X.; Wang, X.; Tang, B. Dual-Channel Imaging of Amyloid-beta Plaques and Peroxynitrite To Illuminate Their Correlations in Alzheimer's Disease Using a Unimolecular Two-Photon Fluorescent Probe. *Anal. Chem.* **2021**, *93*, 15088–15095. [[CrossRef](#)]
51. Wang, P.; Yu, L.; Gong, J.; Xiong, J.; Zi, S.; Xie, H.; Zhang, F.; Mao, Z.; Liu, Z.; Kim, J.S. An Activity-Based Fluorescent Probe for Imaging Fluctuations of Peroxynitrite (ONOO(-)) in the Alzheimer's Disease Brain. *Angew. Chem. Int. Ed. Engl.* **2022**, *61*, e202206894. [[CrossRef](#)] [[PubMed](#)]
52. He, Z.; Liu, D.; Liu, Y.; Li, X.; Shi, W.; Ma, H. Golgi-Targeted Fluorescent Probe for Imaging NO in Alzheimer's Disease. *Anal. Chem.* **2022**, *94*, 10256–10262. [[CrossRef](#)] [[PubMed](#)]
53. Lai, Y.; Dang, Y.; Sun, Q.; Pan, J.; Yu, H.; Zhang, W.; Xu, Z. Design of an activatable NIR-II nanoprobe for the in vivo elucidation of Alzheimer's disease-related variations in methylglyoxal concentrations. *Chem. Sci.* **2022**, *13*, 12511–12518. [[CrossRef](#)] [[PubMed](#)]
54. Yang, Y.; Zhang, L.; Wang, J.; Cao, Y.; Li, S.; Qin, W.; Liu, Y. Diagnosis of Alzheimer's Disease and In Situ Biological Imaging via an Activatable Near-Infrared Fluorescence Probe. *Anal. Chem.* **2022**, *94*, 13498–13506. [[CrossRef](#)] [[PubMed](#)]
55. Elbatrawy, A.A.; Hyeon, S.J.; Yue, N.; Osman, E.E.A.; Choi, S.H.; Lim, S.; Kim, Y.K.; Ryu, H.; Cui, M.; Nam, G. "Turn-On" Quinoline-Based Fluorescent Probe for Selective Imaging of Tau Aggregates in Alzheimer's Disease: Rational Design, Synthesis, and Molecular Docking. *ACS Sens.* **2021**, *6*, 2281–2289. [[CrossRef](#)]
56. Bloem, B.R.; Okun, M.S.; Klein, C. Parkinson's disease. *Lancet* **2021**, *397*, 2284–2303. [[CrossRef](#)]
57. Jenner, P. Oxidative stress in Parkinson's disease. *Ann. Neurol.* **2003**, *53*, S26–S38. [[CrossRef](#)]
58. Sun, Q.; Xu, J.; Ji, C.; Shaibani, M.S.S.; Li, Z.; Lim, K.; Zhang, C.; Li, L.; Liu, Z. Ultrafast Detection of Peroxynitrite in Parkinson's Disease Models Using a Near-Infrared Fluorescent Probe. *Anal. Chem.* **2020**, *92*, 4038–4045. [[CrossRef](#)] [[PubMed](#)]
59. Kang, H.; Shu, W.; Yu, J.; Gao, M.; Han, R.; Jing, J.; Zhang, R.; Zhang, X. A near-infrared fluorescent probe for ratiometric imaging peroxynitrite in Parkinson's disease model. *Sens. Actuators B Chem.* **2022**, *359*, 131393. [[CrossRef](#)]
60. Wang, H.Q.; Takahashi, R. Expanding Insights on the Involvement of Endoplasmic Reticulum Stress in Parkinson's Disease. *Antioxid. Redox Signal.* **2007**, *9*, 553–561. [[CrossRef](#)]
61. Yan, M.; Fang, H.; Wang, X.; Xu, J.; Zhang, C.; Xu, L.; Li, L. A two-photon fluorescent probe for visualizing endoplasmic reticulum peroxynitrite in Parkinson's disease models. *Sens. Actuators B Chem.* **2021**, *328*, 129003. [[CrossRef](#)]
62. Rao, G.N.; Berk, B.C. Active oxygen species stimulate vascular smooth muscle cell growth and proto-oncogene expression. *Circ. Res.* **1992**, *70*, 593–599. [[CrossRef](#)]
63. Liu, Y.; Bai, L.; Li, Y.; Ni, Y.; Xin, C.; Zhang, C.; Liu, J.; Liu, Z.; Li, L.; Huang, W. Visualizing hydrogen peroxide in Parkinson's disease models via a ratiometric NIR fluorogenic probe. *Sens. Actuators B Chem.* **2019**, *279*, 38–43. [[CrossRef](#)]
64. Schapira, A.H.V. Mitochondria in the aetiology and pathogenesis of Parkinson's disease. *Lancet Neurol.* **2008**, *7*, 97–109. [[CrossRef](#)]
65. Li, H.; Xin, C.; Zhang, G.; Han, X.; Qin, W.; Zhang, C.-W.; Yu, C.; Jing, S.; Li, L.; Huang, W. A mitochondria-targeted two-photon fluorogenic probe for the dual-imaging of viscosity and H<sub>2</sub>O<sub>2</sub> levels in Parkinson's disease models. *J. Mater. Chem. B* **2019**, *7*, 4243–4251. [[CrossRef](#)]
66. Yang, J.; Wang, L.; Su, Y.; Shen, L.; Gao, X.; Shi, L.; Zhu, X. Color-convertible fluorescent nanoprobe for Parkinson's disease diagnosis. *Chem. Eng. J.* **2022**, *429*, 132368. [[CrossRef](#)]
67. Hou, J.-T.; Kwon, N.; Wang, S.; Wang, B.; He, X.; Yoon, J.; Shen, J. Sulfur-based fluorescent probes for HOCl: Mechanisms, design, and applications. *Coord Chem. Rev.* **2022**, *450*, 214232. [[CrossRef](#)]

68. Chen, J.; Lu, Y.; Wu, Y.; Chen, Z.; Liu, X.; Zhang, C.; Sheng, J.; Li, L.; Chen, W.; Song, X. De Novo Design of a Robust Fluorescent Probe for Basal HClO Imaging in a Mouse Parkinson's Disease Model. *ACS Chem. Neurosci.* **2021**, *12*, 4058–4064. [[CrossRef](#)] [[PubMed](#)]
69. Li, S.; Huo, F.; Yin, C. NIR fluorescent probe for dual-response viscosity and hydrogen sulfide and its application in Parkinson's disease model. *Dyes Pigm.* **2022**, *197*, 109825. [[CrossRef](#)]
70. Disease, G.B.D.; Injury, I.; Prevalence, C. Global, regional, and national incidence, prevalence, and years lived with disability for 354 diseases and injuries for 195 countries and territories, 1990–2017: A systematic analysis for the Global Burden of Disease Study 2017. *Lancet* **2018**, *392*, 1789–1858. [[CrossRef](#)]
71. Bhatt, S.; Nagappa, A.N.; Patil, C.R. Role of oxidative stress in depression. *Drug Discov. Today* **2020**, *25*, 1270–1276. [[CrossRef](#)]
72. Berk, M.; Copolov, D.L.; Dean, O.; Lu, K.; Jeavons, S.; Schapkaitz, I.; Anderson-Hunt, M.; Bush, A.I. N-Acetyl Cysteine for Depressive Symptoms in Bipolar Disorder—A Double-Blind Randomized Placebo-Controlled Trial. *Biol. Psychiatry* **2008**, *64*, 468–475. [[CrossRef](#)]
73. Zhang, Y.; Wang, X.; Bai, X.; Li, P.; Su, D.; Zhang, W.; Zhang, W.; Tang, B. Highly Specific Cys Fluorescence Probe for Living Mouse Brain Imaging via Evading Reaction with Other Biothiols. *Anal. Chem.* **2019**, *91*, 8591–8594. [[CrossRef](#)]
74. Ding, Q.; Tian, Y.; Wang, X.; Li, P.; Su, D.; Wu, C.; Zhang, W.; Tang, B. Oxidative Damage of Tryptophan Hydroxylase-2 Mediated by Peroxisomal Superoxide Anion Radical in Brains of Mouse with Depression. *J. Am. Chem. Soc.* **2020**, *142*, 20735–20743. [[CrossRef](#)]
75. Zhang, W.; Wang, R.; Liu, W.; Wang, X.; Li, P.; Zhang, W.; Wang, H.; Tang, B. Te-containing carbon dots for fluorescence imaging of superoxide anion in mice during acute strenuous exercise or emotional changes. *Chem. Sci.* **2018**, *9*, 721–727. [[CrossRef](#)]
76. Pell, E.J.; Schlaghauser, C.D.; Arteca, R.N. Ozone-induced oxidative stress: Mechanisms of action and reaction. *Physiol. Plant* **1997**, *100*, 264–273. [[CrossRef](#)]
77. Li, P.; Wang, J.; Wang, X.; Ding, Q.; Bai, X.; Zhang, Y.; Su, D.; Zhang, W.; Zhang, W.; Tang, B. In situ visualization of ozone in the brains of mice with depression phenotypes by using a new near-infrared fluorescence probe. *Chem. Sci.* **2019**, *10*, 2805–2810. [[CrossRef](#)]
78. Lipinski, B. Hydroxyl Radical and Its Scavengers in Health and Disease. *Oxid. Med. Cell Longev.* **2011**, *2011*, 809696. [[CrossRef](#)] [[PubMed](#)]
79. Wang, X.; Li, P.; Ding, Q.; Wu, C.; Zhang, W.; Tang, B. Illuminating the Function of the Hydroxyl Radical in the Brains of Mice with Depression Phenotypes by Two-Photon Fluorescence Imaging. *Angew. Chem. Int. Ed.* **2019**, *58*, 4674–4678. [[CrossRef](#)] [[PubMed](#)]
80. Martinowich, K.; Manji, H.; Lu, B. New insights into BDNF function in depression and anxiety. *Nat. Neurosci.* **2007**, *10*, 1089–1093. [[CrossRef](#)]
81. Li, P.; Guo, X.; Bai, X.; Wang, X.; Ding, Q.; Zhang, W.; Zhang, W.; Tang, B. Golgi Apparatus Polarity Indicates Depression-Like Behaviors of Mice Using in Vivo Fluorescence Imaging. *Anal. Chem.* **2019**, *91*, 3382–3388. [[CrossRef](#)] [[PubMed](#)]
82. Carroll, R.C.; Zukin, R.S. NMDA-receptor trafficking and targeting: Implications for synaptic transmission and plasticity. *Trends Neurosci.* **2002**, *25*, 571–577. [[CrossRef](#)] [[PubMed](#)]
83. Frederickson, C.J.; Koh, J.-Y.; Bush, A.I. The neurobiology of zinc in health and disease. *Nat. Rev. Neurosci.* **2005**, *6*, 449–462. [[CrossRef](#)] [[PubMed](#)]
84. Traynelis, S.F.; Cull-Candy, S.G. Pharmacological properties and H<sup>+</sup> sensitivity of excitatory amino acid receptor channels in rat cerebellar granule neurons. *J. Physiol.* **1991**, *433*, 727–763. [[CrossRef](#)]
85. Wang, X.; Bai, X.; Su, D.; Zhang, Y.; Li, P.; Lu, S.; Gong, Y.; Zhang, W.; Tang, B. Simultaneous Fluorescence Imaging Reveals N-Methyl-d-aspartic Acid Receptor Dependent Zn(2+)/H(+) Flux in the Brains of Mice with Depression. *Anal. Chem.* **2020**, *92*, 4101–4107. [[CrossRef](#)]
86. Zhu, H.; Jia, P.; Wang, X.; Tian, Y.; Liu, C.; Li, X.; Wang, K.; Li, P.; Zhu, B.; Tang, B. In Situ Observation of Lysosomal Hypobromous Acid Fluctuations in the Brain of Mice with Depression Phenotypes by Two-Photon Fluorescence Imaging. *Anal. Chem.* **2022**, *94*, 11783–11790. [[CrossRef](#)]
87. Moret, C.; Briley, M. The importance of norepinephrine in depression. *Neuropsychiatr. Dis. Treat.* **2011**, *7*, 9–13. [[CrossRef](#)]
88. Zhou, N.; Huo, F.; Yue, Y.; Yin, C. Specific Fluorescent Probe Based on “Protect-Deprotect” To Visualize the Norepinephrine Signaling Pathway and Drug Intervention Tracers. *J. Am. Chem. Soc.* **2020**, *142*, 17751–17755. [[CrossRef](#)]
89. Walczak-Nowicka, Ł.J.; Herbet, M. Acetylcholinesterase Inhibitors in the Treatment of Neurodegenerative Diseases and the Role of Acetylcholinesterase in their Pathogenesis. *Int. J. Mol. Sci.* **2021**, *22*, 9290. [[CrossRef](#)]
90. Wang, X.; Li, P.; Ding, Q.; Wu, C.; Zhang, W.; Tang, B. Observation of Acetylcholinesterase in Stress-Induced Depression Phenotypes by Two-Photon Fluorescence Imaging in the Mouse Brain. *J. Am. Chem. Soc.* **2019**, *141*, 2061–2068. [[CrossRef](#)]
91. Zhang, W.; Liu, X.; Li, P.; Zhang, W.; Wang, H.; Tang, B. In Situ Fluorescence Imaging of the Levels of Glycosylation and Phosphorylation by a MOF-Based Nanoprobe in Depressed Mice. *Anal. Chem.* **2020**, *92*, 3716–3721. [[CrossRef](#)] [[PubMed](#)]
92. van Os, J.; Kenis, G.; Rutten, B.P.F. The environment and schizophrenia. *Nature* **2010**, *468*, 203–212. [[CrossRef](#)] [[PubMed](#)]
93. Ide, M.; Ohnishi, T.; Toyoshima, M.; Balan, S.; Maekawa, M.; Shimamoto-Mitsuyama, C.; Iwayama, Y.; Ohba, H.; Watanabe, A.; Ishii, T.; et al. Excess hydrogen sulfide and polysulfides production underlies a schizophrenia pathophysiology. *EMBO Mol. Med.* **2019**, *11*, e10695. [[CrossRef](#)]

94. Geng, Y.; Zhang, G.; Chen, Y.; Peng, Y.; Wang, X.; Wang, Z. Si-Rhodamine Derivatives for Brain Fluorescence Imaging and Monitoring of H(2)S in the Brain of Schizophrenic Mice before and after Treatment. *Anal. Chem.* **2022**, *94*, 1813–1822. [[CrossRef](#)] [[PubMed](#)]
95. Pernot, P.; Mothet, J.-P.; Schuvailo, O.; Soldatkin, A.; Pollegioni, L.; Pilone, M.; Adeline, M.-T.; Cespuglio, R.; Marinesco, S. Characterization of a Yeast d-Amino Acid Oxidase Microbiosensor for d-Serine Detection in the Central Nervous System. *Anal. Chem.* **2008**, *80*, 1589–1597. [[CrossRef](#)]
96. Sakamoto, T.; Odera, K.; Onozato, M.; Sugasawa, H.; Takahashi, R.; Fujimaki, Y.; Fukushima, T. Direct Fluorescence Evaluation of d-Amino Acid Oxidase Activity Using a Synthetic d-Kynurenine Derivative. *Anal. Chem.* **2022**, *94*, 14530–14536. [[CrossRef](#)]
97. Herculano-Houzel, S.; Avelino-de-Souza, K.; Neves, K.; Porfirio, J.; Messeder, D.; Mattos Feijo, L.; Maldonado, J.; Manger, P.R. The elephant brain in numbers. *Front. Neuroanat.* **2014**, *8*, 46. [[CrossRef](#)]
98. Zhu, S.; Tian, R.; Antaris, A.L.; Chen, X.; Dai, H. Near-Infrared-II Molecular Dyes for Cancer Imaging and Surgery. *Adv. Mater.* **2019**, *31*, 1900321. [[CrossRef](#)]

**Disclaimer/Publisher's Note:** The statements, opinions and data contained in all publications are solely those of the individual author(s) and contributor(s) and not of MDPI and/or the editor(s). MDPI and/or the editor(s) disclaim responsibility for any injury to people or property resulting from any ideas, methods, instructions or products referred to in the content.